

DESI Strong Lens Foundry V: A Sample of *HST*-Observed Strong Lenses Modeled with GIGA-Lens

XIAOSHENG HUANG,^{1,2} DAVID ÁLVAREZ-GARCÍA,^{2,3} MÓNICA ÚBEDA,^{2,3} VIKRAM BHAMRE,⁴
SEAN XU,^{4,2} S. BALTASAR,^{2,3} N. RATIER-WERBIN,^{2,3} F. URCELAY,⁵ S. AGARWAL,⁶ A. CIKOTA,⁷
YUAN-MING HSU,⁸ E. LIN,⁴ D. J. SCHLEGEL,² E. SILVER,⁹ C. J. STORFER,¹⁰ AND
M. TAMARGO-ARIZMENDI²

¹*Department of Physics & Astronomy, University of San Francisco, San Francisco, CA 94117, USA*

²*Physics Division, Lawrence Berkeley National Laboratory, 1 Cyclotron Road, Berkeley, CA 94720, USA*

³*Department of Physics, Complutense University of Madrid, 28040 Madrid, Spain*

⁴*Department of Physics, University of California, Berkeley, Berkeley, CA 94720, USA*

⁵*Institute of Astrophysics, Pontificia Universidad Católica de Chile, Santiago, Chile*

⁶*University of Chicago, Department of Astronomy, Chicago, IL 60615, USA*

⁷*Gemini Observatory / NSF's NOIRLab, Casilla 603, La Serena, Chile*

⁸*Department of Physics, National Taiwan University, No. 1, Section 4, Roosevelt Road, Taipei 106319, Taiwan*

⁹*Department of Physics, Harvard University, Cambridge, MA 02138, USA*

¹⁰*Institute for Astronomy, University of Hawai'i, Honolulu, HI 96822-1897, USA*

Submitted to ApJ

ABSTRACT

We present six galaxy-scale strong lenses with *HST* imaging modeled using GIGA-Lens. This is Paper V of the DESI Strong Lens Foundry series. These systems were discovered in the DESI Legacy Imaging Surveys using ML/AI methods and confirmed with DESI, Keck/NIRES, and VLT/MUSE spectroscopy. They span $z_d = 0.39 - 1.1$ and $z_s = 1.4 - 3.3$. This is the first *HST* strong lens sample modeled with full forward modeling—all lens and source parameters sampled simultaneously in a single inference—with explicit convergence validation using both \hat{R} and effective sample size (ESS) for each system. All inferred parameters satisfy $\hat{R} < 1.1$ and $\text{ESS} \gtrsim 10,000$, demonstrating that GIGA-Lens achieves statistically robust inference even for some of the most complex galaxy-scale lenses known. These results pave the way for scaling to much larger, high-resolution strong lens samples from *HST*, *Euclid*, *JWST*, and *Roman*. Convergence-validated modeling will be critical for key science goals, including constraining the mass-density profile of galaxies, detecting low-mass dark matter (sub)halos, and delivering precise and accurate cosmological constraints.

Keywords: galaxies: high-redshift – gravitational lensing: strong

1. INTRODUCTION

Strong gravitational lensing systems are a powerful tool for astrophysics and cosmology. They have been used to study how dark matter is distributed in galaxies and galaxy clusters (e.g., Kochanek 1991; Blandford & Narayan 1992; Broadhurst et al. 2000; Koopmans & Treu 2002; Bolton et al. 2006; Koopmans et al. 2006; Brada et al. 2008; Vegetti & Koopmans 2009; Huang et al. 2009; Jullo et al. 2010; Tessore et al. 2016; Jauzac et al. 2018; Shajib et al. 2019; Meneghetti et al. 2020; O’Donnell et al. 2025). Furthermore, carefully modeling the mass profiles of galaxy-scale strong lenses for a large number of lensing systems over a wide range of redshifts makes it possible to study the structural evolution of massive elliptical galaxies (e.g., Bolton et al. 2012; Filipp et al. 2023).

They are uniquely suited to probe dark matter substructure beyond the local universe and line-of-sight low-mass halos (e.g., Vegetti et al. 2014; Hezaveh et al. 2016; Vegetti et al. 2018; Ritondale et al. 2019; Diaz Rivero & Dvorkin 2020; Çağan Şengül et al. 2022; Nierenberg et al. 2023), to test the predictions of the cold dark matter (CDM) model.

Recent measurements of the Hubble constant H_0 span a range of $\sim 10\%$ (e.g., Abbott et al. 2017, 2018; Riess et al. 2019; Wong et al. 2019; Freedman et al. 2019, 2020; Planck Collaboration et al. 2020; Khetan et al. 2020; Philcox et al. 2020; Choi et al. 2020; Dhawan et al. 2023), and significant tension between predictions for H_0 based on early-universe observables and direct late-universe measurements remain (e.g., Verde et al. 2019). Multiply-lensed supernovae (SNe) and quasars have been used for measuring time delays and H_0 (Refsdal 1964; Treu 2010; Oguri & Marshall 2010; Wong et al. 2019; Suyu et al. 2023; Kelly et al. 2023; Pascale et al. 2025).

Furthermore time delay H_0 measurements are a powerful complement to other independent measurements of the dark energy equation of state (e.g., Linder 2011; Treu & Marshall 2016; Pierel et al. 2021). In addition, multi-source-plane systems can constrain cosmology by providing angular diameter distance ratios along a single line of sight (e.g., Collett & Auger 2014; Sharma & Linder 2022; Sharma et al. 2023). Finally, for nearby strong lensing galaxies, extra-galactic tests of General Relativity can be performed by combining lens modeling with spatially resolved stellar kinematic observations (Collett et al. 2018).

The DESI Legacy Surveys¹ (Dey et al. 2019, Schlegel et al. in prep), for which at least z band is observed with a 4-m telescope, covers $>20,000$ deg², four times the size of the Dark Energy Survey (The Dark Energy Survey Collaboration 2005) footprint. We identified ~ 4000 new strong lenses in the Legacy Surveys Data Release 7, 8, 9, and 10 (Huang et al. 2020; Huang et al. 2021; Storfer et al. 2024; Inchausti et al. 2025, respectively) by using residual neural networks (and EfficientNet for the DR10 search). We have also found 436 lensed quasars (Dawes et al. 2023) using autocorrelation for a lensed quasar candidate sample. Very recently, we have found over 6000 lens candidates in the DESI spectroscopic data (Hsu et al. 2025; Karp et al. 2025). The entire catalog of these lens candidates can be found on our project website.²

With so many lens discoveries, a fast and robust modeling pipeline is needed. We therefore developed **GIGA-Lens** (Gu et al. 2022). A GPU-accelerated, fully forward-modeling Bayesian pipeline

¹ <http://www.legacysurvey.org/>

² <https://sites.google.com/usfca.edu/neuralens/>

that can speed up the lens modeling time by two orders of magnitude. In [Cikota et al. \(2023\)](#), we applied GIGA-Lens to a observed lensing system, DESI J253.2534+26.8843. It was then applied to a group-scaled strong lens (DES J0248-3955), also using ground-based imaging data ([Urcelay et al. 2025](#)). Most recently we applied it to a system with *HST* data, DESI J165.4754-06.0423 ([Huang et al. 2025a](#), Paper I in this series).

This is paper V of the DESI Strong Lens Foundry paper series. In this paper, we present six lensing systems that have been fully confirmed with both spectroscopy and *HST* imaging. These systems were first identified as lens candidates in ([Huang et al. 2020](#); [Huang et al. 2021](#), henceforth, H20, H21). As mentioned in [Huang et al. \(2025b\)](#), Paper II of this series, for systems with candidate status, we follow the naming convention of “DESI-” followed by the RA and Dec (with a sign prefix) in decimal format to the fourth decimal place (with rounding) for both coordinates. Such a naming scheme is easy to parse and precise to $< 1''$. With full confirmation, which is the case for the systems in this work, we follow the official DESI naming convention of “DESI J” (note the space) followed by RA and Dec (with a sign prefix) in decimal format to the fourth decimal place (with truncation) for both coordinates. Simply put, the presence of “J” indicates a system has now been fully confirmed. This paper is organized as follows. The six systems from our *Hubble Space Telescope* SNAP program to be modeled in this work are presented in § 2, followed by a brief description of the spectroscopic observations in § 3. In § 4, we highlight two representative systems modeled with GIGA-Lens, while the results for the remaining systems are provided in Appendix B (with the effective PSF generation described in Appendix A). We discuss our results in § 5 and conclude in § 6.

2. *Hubble Space Telescope* SNAP PROGRAM

We presented our *Hubble* SNAP program GO-15867 (PI: X. Huang) in Paper I in this series. This program followed up on a subset of the lens candidates found in H20 and H21, using the DESI Legacy Imaging Surveys data. All targets have 3×399.23 sec exposure, for a total of 1197.7 sec, on WFC3 using the F140W filter in the NIR channel. The targets were approximately centered in the WFC3 aperture, with no CR split, because we wanted to keep read noise down. Of the 112 systems submitted to *HST*, a total of 53 were targeted. Two of them were not successfully observed due to the loss of the guide star. The native pixel size is $0.13''$, and each image is drizzled to $0.065''$. The six systems that will be modeled in the paper are presented in Figure 1.

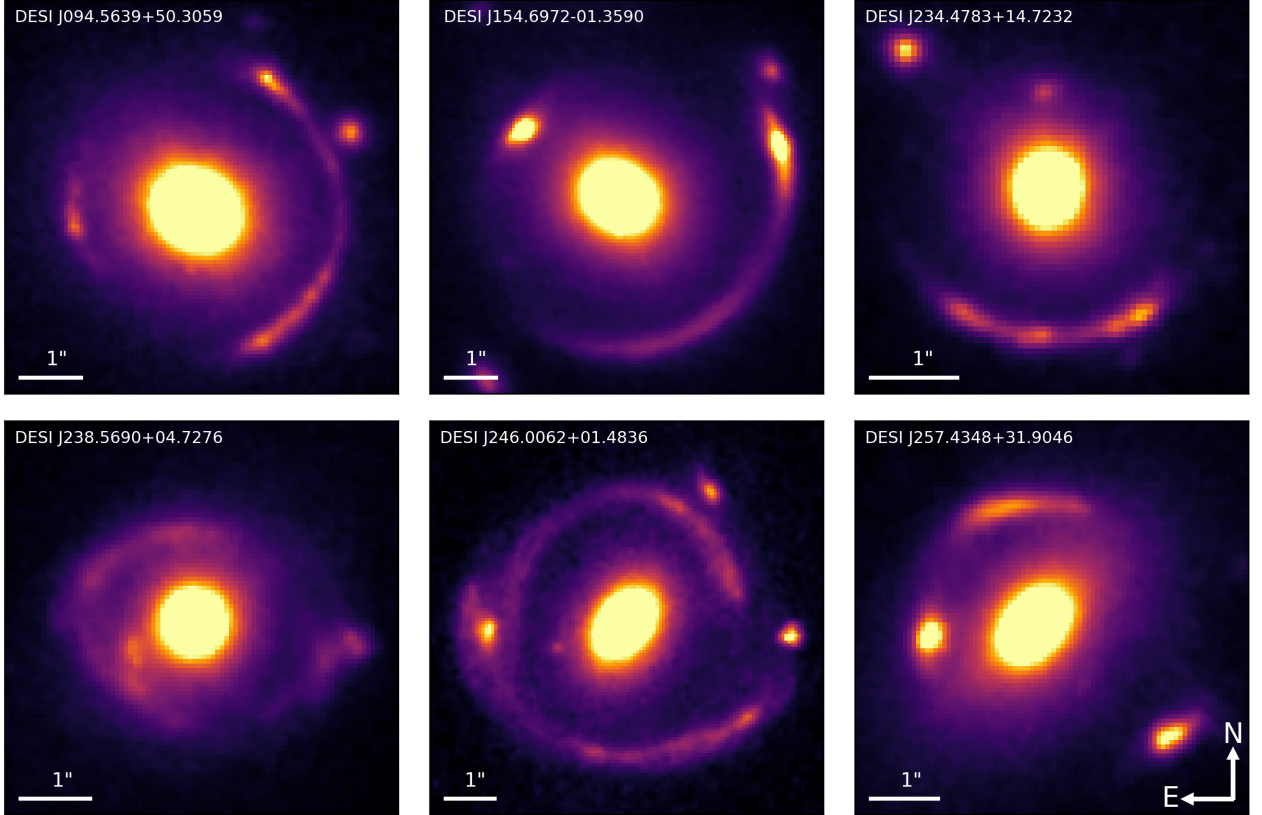


Figure 1. Six systems observed by the *HST* SNAP program GO-15867 modeled in this paper. The naming convention is RA and Dec in decimal format. North is up, and East to the left. The systems are arranged in ascending RA.

3. SPECTROSCOPIC OBSERVATIONS

The DESI Strong Lens Secondary Target program (introduced in Paper II in this series) has observed a large fraction of our lens candidates. The success rate of obtaining redshifts for lensing galaxies by DESI is high. These are nearly always bright elliptical galaxies with a number of identifiable features in the optical range, typically absorption lines and the 4000 Å break. For lensed sources, some of the spectra have no clear features, likely due to the fact that they are too faint and/or their redshifts place key spectral features outside the optical range. Lensed sources are typically star forming galaxies for which the [O II] doublet emission feature is often used to anchor redshift fits. This makes redshift measurements in the optical range for $z_s \gtrsim 1.6$ challenging.³ For these systems, we determine their redshifts from our on-going Keck NIRES program (Agarwal et al. 2025, Paper III in this series; and Storfer, Tamargo et al., Paper VI, in prep.). Finally some of our systems are being observed by a VLT MUSE program (PI: A. Cikota). Most of these are only observable from the southern hemisphere. But our MUSE program does target some systems that are in the DESI strong lens program but not yet observed by DESI, because they are of high priority (e.g., Cikota et al. 2023). The MUSE results are presented in Paper IV of this series (Lin et al. 2025).

³ It is true that for $z_s \gtrsim 2.0$, Ly- α will be in the optical range, though this feature is not always present.

4. LENS MODELING

In Paper I, as a demonstration, we used the open-source **GIGA-Lens**⁴ framework (Gu et al. 2022, Gu22) to model one lens system with *HST* data, DESI J165.6876-06.0423. In the following, we present lens models for this and six additional systems in Table 1, arranged in increasing lens redshift. The effective PSF generation is described in Appendix § A. In this section, we present the lens modeling results for two systems. For DESI J234.4783+14.7232 (§ 4.1), we fix five light profile parameters for a field galaxy based on preliminary modeling, and then optimize and sample the remaining 36 parameters *simultaneously* in the main modeling process. Such a field galaxy has little to no impact on the lensing of the background source. To emphasize this, we refer to these field galaxies as environmental galaxies throughout this work. For DESI J238.5690+04.7276 (§ 4.2), we do not even fix the parameters of an environmental galaxy: all 38 are modeled and sampled simultaneously. The remaining systems are presented in Appendix B.

GIGA-Lens is a fully forward-modeling Bayesian lens modeling pipeline. Briefly, it consists of three stages: finding the maximum a posteriori (MAP) for the lensing parameters via multi-start gradient descent, determining a surrogate multidimensional Gaussian covariance matrix for these parameters using stochastic variational inference (SVI), and finally sampling with Hamiltonian Monte Carlo (HMC). All three stages use gradient descent with automatic differentiation and take advantage of GPU acceleration.

Our mass model consists of an elliptical power law (EPL) for the lens mass profile and external shear. The Einstein radius is denoted θ_E (arcsec), and γ is the EPL mass-slope parameter. (x, y) denote the center coordinates, specified independently for the lens mass, lens light, and source light. $(\gamma_{1,\text{ext}}, \gamma_{2,\text{ext}})$ are the external shear components. The parameters ϵ_1 and ϵ_2 specify the eccentricities. We model lens light with one or more Sérsic profiles. For source light, we use Sérsic profiles and/or shapelets (Birrer et al. 2015). For the lens and source surface brightness scaling, we either model the light intensities as parameters or solve for them by linear inversion. Both are mathematically justified. A systematic, side-by-side evaluation of these approaches—particularly their impact on uncertainties—will be explored in a future study.

We aim for 1) full forward modeling (the modeling of all lens and source parameters at the same time, instead of taking a staged approach) and 2) statistical convergence. Both goals have been achieved for all seven systems (including DESI J165.6876-06.0423 from Paper I).

We apply the two widely used diagnostics for convergence. 1) the potential scale reduction factor (PSRF, or \hat{R}), also known as the Gelman-Rubin statistic, which compares the inter- and intra-chain estimates for model parameters. 2) The effective sample size (ESS). To achieve good convergence \hat{R} needs to be below 1.1 (Gelman & Rubin 1992; Gelman et al. 2014). This indicates that the between- and within-chain estimates are in good agreement, or the chains have “mixed well”. In addition, the ESS generally needs to be higher than 1000 (e.g., Mandel et al. 2022). For all seven systems, we achieve $\hat{R} < 1.1$ and $\text{ESS} \gtrsim 10,000$, satisfying the convergence criteria. We will present each system in turn.

⁴ <https://github.com/giga-lens/gigalens>

Table 1. Seven Modeled Systems

| System [1] | z_d [2] | z_s [3] | θ_E (") [4] | γ [5] | Modelers [6] | \hat{R}_{ceiling} [7] | Sec [8] | Source Model [9] | Params (tot/fix) [10] |
|------------------------|---------------------|--------------|-------------------------------|----------------------------|-----------------|-----------------------------------|------------|---------------------|---------------------------|
| DESI J154.6972-01.3590 | 0.3884 [§] | 1.4304* | 2.8982 $^{+0.0010}_{-0.0011}$ | 1.411±0.016 | MU | 1.005 | B.1 | 4 Sérsic's | 44/6 |
| DESI J165.6876-06.0423 | 0.4834* | 1.6748 | 2.6263 $^{+0.0017}_{-0.0016}$ | 1.372 $^{+0.023}_{-0.022}$ | SB, NRW | 1.06 | B.2 | Sérsic+shapelets | 35/0 ($n_{max} = 6$) |
| DESI J094.5639+50.3059 | 0.552* [‡] | 3.3332 | 2.295±0.001 | 2.548 $^{+0.043}_{-0.042}$ | VB | 1.09 | B.3 | 2 Sérsic's | 44/6 |
| DESI J234.4783+14.7232 | 0.7313* | 2.4780 | 1.548 $^{+0.004}_{-0.003}$ | 2.057 $^{+0.028}_{-0.032}$ | DA | 1.009 | 4.1 | 2 Sérsic's | 41/5 |
| DESI J257.4348+31.9046 | 0.7464* | 2.1200 | 1.9899±0.0024 | 2.066±0.023 | DA | 1.001 | B.4 | shapelets | 29/0 ($n_{max} = 3$) |
| DESI J238.5690+04.7276 | 0.7768* | 1.7210 | 1.475 $^{+0.003}_{-0.002}$ | 1.937 $^{+0.019}_{-0.020}$ | SX | 1.08 | 4.2 | 2 Sérsic's | 38/0 |
| DESI J246.0062+01.4836 | 1.092 [°] | 2.3685 | 2.698±0.001 | 2.616±0.017 | DA, SX | 1.037 | B.5 | 5 Sérsic's | 78/28 |

NOTE—Column [1]: System names arranged in ascending order of lens redshifts. [2] and [3] show lens redshifts (z_d) and source redshifts (z_s), respectively. The redshifts without a superscript are obtained from Keck NIRES, with the facilities used to obtain the rest shown at the bottom of these notes. [4]: Best-fit Einstein radii. [5]: Best-fit mass density slope. [6]: Modelers, with XH for every system. [7]: The ceiling of \hat{R} for each system, i.e., the \hat{R} for all parameters are lower than the value shown for that system. [8]: The section that describes the modeling of each system. The model for DESI J165.6876-06.0423 was presented in Paper I and was summarized in this work. [9]: Source light model. For the cases where we use shapelets, n_{max} is given. [10]: *We emphasize that only the light profile parameters of environmental galaxies in the cutout image are fixed based on preliminary modeling, and only for four of the systems.* In each of these cases, 5 - 6 parameters are fixed, except for DESI J246.0062+01.4836, which has an especially complex environment. For DESI J165.6876-06.0423 and DESI J238.5690+04.7276, even the environmental galaxies are included in the full forward modeling. DESI J257.4348+31.9046 does not have environmental galaxies bright enough to require modeling. Finally, the effective sample size (ESS) for HMC is $\gtrsim 10,000$ for all systems.

* DESI; [§] SDSS; [‡] Lick Kast; and [°] VLT MUSE.

4.1. DESI J234.4783+14.7232

DESI J234.4783+14.7232⁵ was discovered in H21, with a ResNet probability of 0.98, and a human score of 3.0 (out of 4.0), corresponding to a B grade. The lens redshift, $z_d=0.7313$ is from DESI (based on the 4000 Å break, Ca H&K, and [O II] emission). The source redshift, $z_s=2.477$ is from Keck NIRES (Storfer, Tamargo et al., in prep; Paper VI). This system has an Einstein radius of 1.55". We use a cutout with 64×64 pixels and a 33×33 pixel empirical PSF, generated using the procedure outlined in Section A.

DESI J234.4783+14.7232 is shown in Figure 2. We model the lens light with two elliptical Sérsic profiles. We mask a region around its center, with a brightness threshold of 1.0 (100 pixels, or 0.4225 arcsec²). We model the source using two elliptical Sérsic profiles. In addition, we mask four small and faint objects, indicated in Figure 2 by small circles: two to the northwest of image C, one to the south of image C, and one to the northeast of image A. We also mask a very bright object near the top right corner. We model the light of the galaxy (blue arrow in Figure 2) to the upper left of the lensing galaxy with a circular Sérsic profile.

Throughout this work, the first figure for each system uses blue arrows to mark environmental galaxies whose light is modeled (but whose mass is not), while blue circles mark objects that are masked and not modeled. For four of the systems, including this one (see Table 1), these light parameters are then held fixed in the main inference. For two others, these parameters are sampled together with the rest of the model parameters. Finally, for DESI J257.4348+31.9046, there are no environmental galaxies bright enough to be modeled.

⁵ The first mention of each system in the text is hyperlinked to the Legacy Surveys [skyviewer web portal](#).

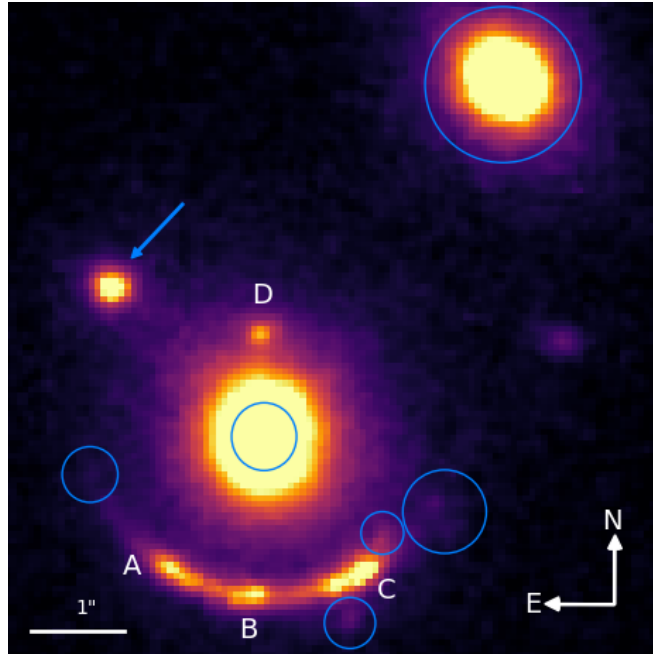


Figure 2. DESI J234.4783+14.7232. The four lensed images are labeled counterclockwise as A, B, C and D. We mask out the light from five faint objects (blue circles). We model the light of the environmental galaxy (blue arrow) to the upper left of the lensing galaxy and then fix its parameters in the main modeling process.

We fit for the light intensities, I_e (instead of using linear inversion). We achieved a reduced $\chi^2 = 0.8789$. The residuals are excellent (Figure 3). The best-fit lens and external shear parameters are presented in Table 2 and their sampling results are shown in Figure 4. The best-fit light parameters are presented in Table 3.

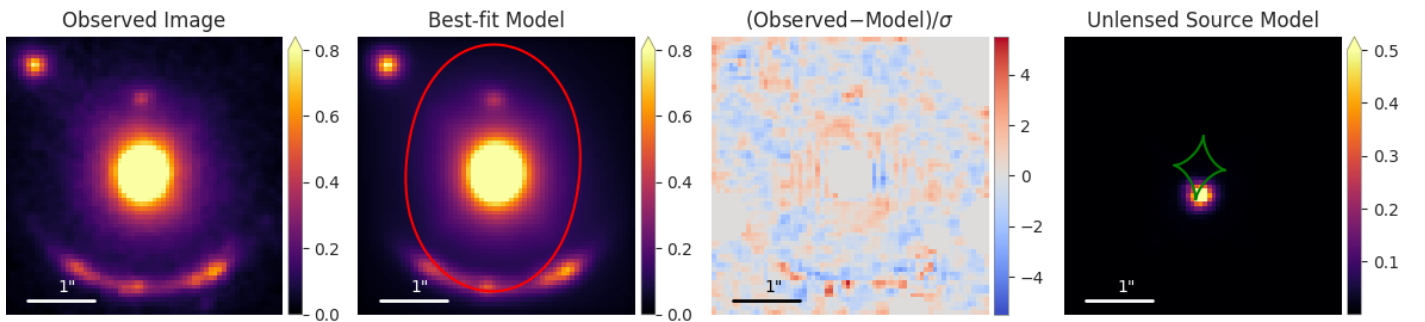


Figure 3. Best-fit Model DESI J234.4783+14.7232. From left to right, we show: the observed Hubble image, our best-fit model with the critical curve, the reduced residual, and the unlensed source with the caustic.

Table 2. Best-fit mass parameters for DESI J234.4783+14.7232.

| θ_E | γ | ϵ_1 | ϵ_2 | x | y | $\gamma_{ext,1}$ | $\gamma_{ext,2}$ |
|------------------------------|---------------------------|--------------------|-------------------------------|-------------------------------|---------------------------|---------------------------|-------------------------------|
| $1.5466^{+0.0062}_{-0.0043}$ | $2.054^{+0.055}_{-0.071}$ | -0.139 ± 0.010 | $-0.0324^{+0.0045}_{-0.0046}$ | $-0.0550^{+0.0045}_{-0.0046}$ | $0.115^{+0.017}_{-0.014}$ | $0.046^{+0.010}_{-0.013}$ | $-0.0509^{+0.0039}_{-0.0038}$ |

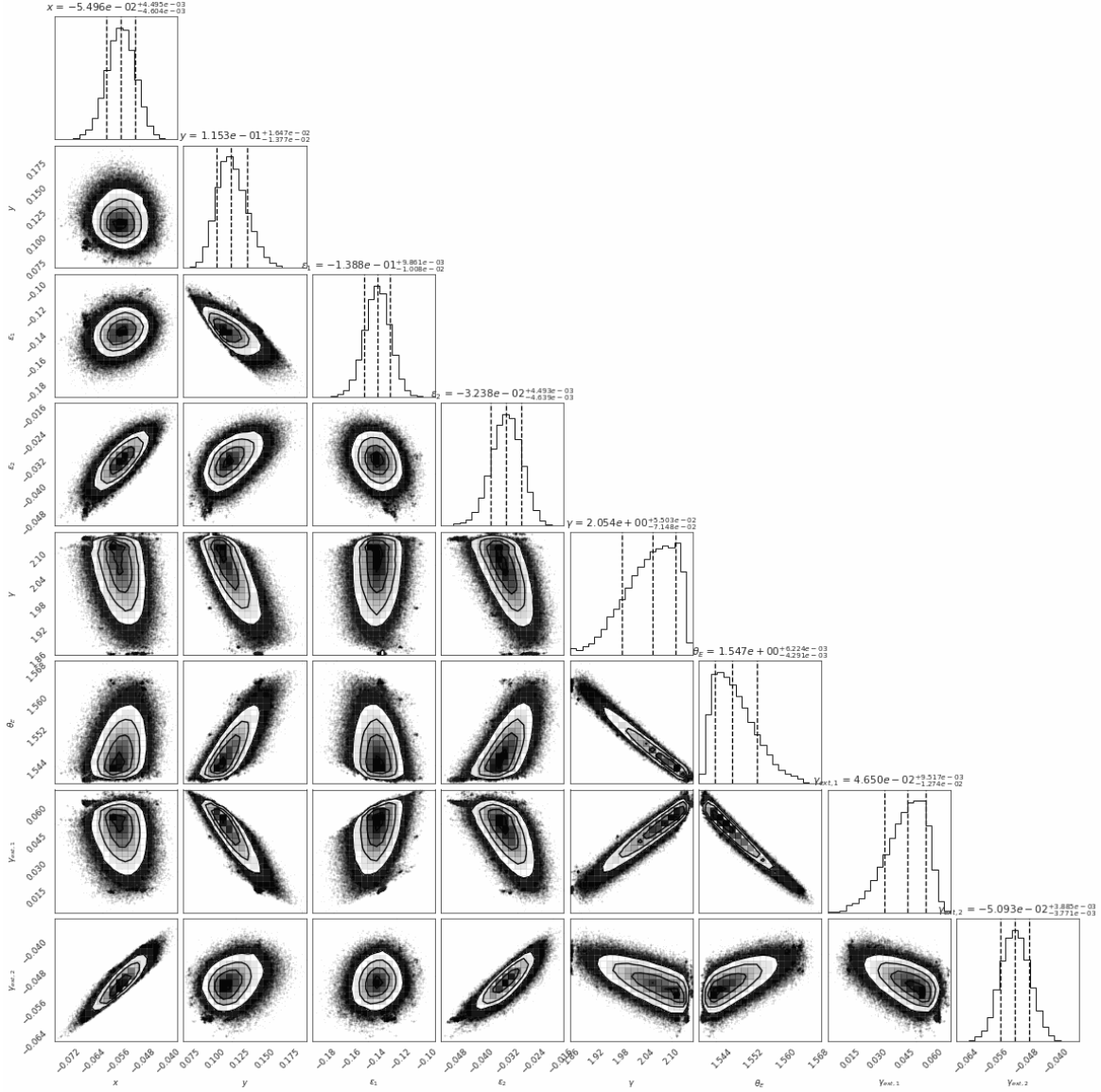
**Figure 4.** Corner plot of the eight mass parameters for DESI J234.4783+14.7232

Table 3. Best-fit light parameters for DESI J234.4783+14.7232.

| Parameter | Lens light | | Source light | |
|--------------|------------------------------|-------------------------------|-------------------------------|-------------------------------|
| | Comp 1 | Comp 2 | Comp 1 | Comp 2 |
| R_e | $3.87^{+0.33}_{-0.28}$ | $0.422^{+0.039}_{-0.035}$ | $0.0341^{+0.0027}_{-0.0026}$ | $0.0475^{+0.0048}_{-0.0044}$ |
| n | $2.22^{+0.19}_{-0.17}$ | $5.80^{+0.28}_{-0.26}$ | $5.71^{+0.22}_{-0.42}$ | $7.82^{+0.14}_{-0.30}$ |
| ϵ_1 | $0.047^{+0.013}_{-0.012}$ | $-0.0969^{+0.0034}_{-0.0035}$ | 0.196 ± 0.022 | $0.255^{+0.029}_{-0.039}$ |
| ϵ_2 | $-0.259^{+0.020}_{-0.021}$ | $0.0217^{+0.0049}_{-0.0047}$ | $0.216^{+0.026}_{-0.027}$ | $0.2962^{+0.0029}_{-0.0060}$ |
| x | $0.136^{+0.022}_{-0.019}$ | -0.0020 ± 0.0005 | $-0.0385^{+0.0045}_{-0.0047}$ | $-0.0939^{+0.0071}_{-0.0074}$ |
| y | $0.0706^{+0.0091}_{-0.0087}$ | 0.0340 ± 0.0006 | $-0.298^{+0.033}_{-0.024}$ | $-0.281^{+0.032}_{-0.024}$ |
| I_e | $2.05^{+0.28}_{-0.25}$ | 111^{+17}_{-15} | 198^{+34}_{-28} | $14.7^{+2.6}_{-2.2}$ |

Figure 5 shows the two components of the source, with the first one (left column) being considerably brighter than the second (right column).

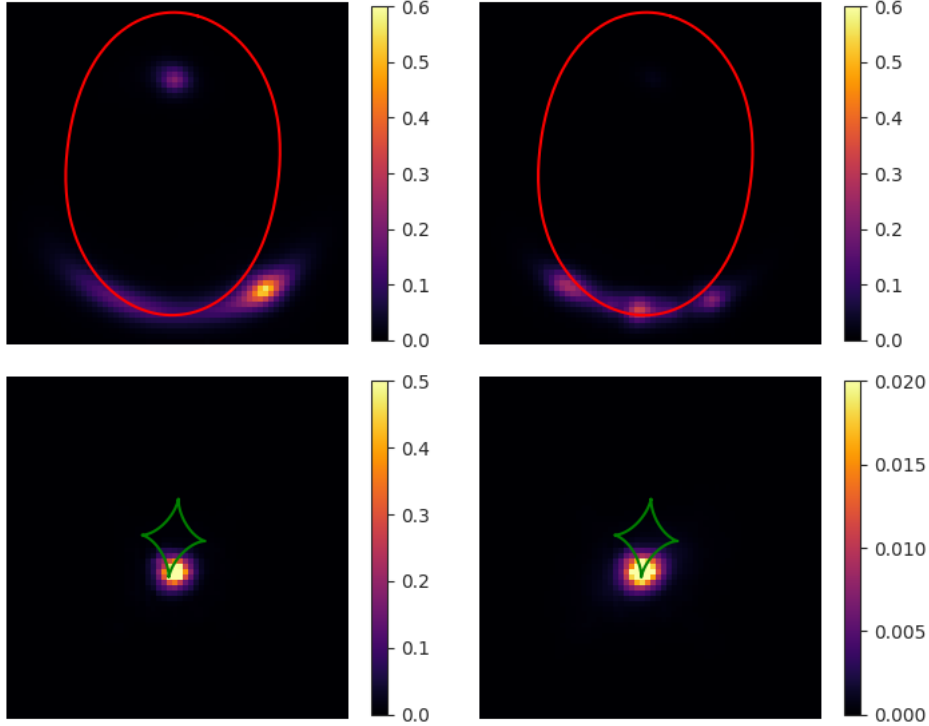


Figure 5. Source light Sérsic components in the lensed and unlensed plane for DESI J234.4783+14.7232 from left to right, component 1 and 2, respectively.

For MAP, we used 10,000 samples (n_{MAP} in Gu22) and 2000 steps. It ran for 2 minutes and 33 seconds. SVI was configured with 4000 samples (n_{VI} in Gu22) and 4000 steps, using a quadratic

transition through the first 3500 steps from an initial learning rate of 0 to a -3×10^{-3} final rate (for details, see Gu22). It ran for 2 minutes and 41 seconds. For HMC, we used 8 chains, 1500 burn-in steps, and 30,000 total results, with 20 steps between samples. The target acceptance probability was set at 0.75, the initial step size at $\epsilon = 0.03$, $L = 3$ initial leapfrog steps, and a maximum of 30 leapfrog steps. It ran for 11 hours and 43 minutes. *All \hat{R} values are below 1.01.* We achieve an average \hat{R} of 1.0020, with the maximum value being 1.0087. We note that for this system we tested how low we could drive \hat{R} . If we were satisfied with merely presentable corner plots, or even simply requiring $\hat{R} < 1.1$, the total execution time would have been an order of magnitude lower.

We determine the Einstein radius of the lens to be $\theta_E = 1.5466''^{+0.0062}_{-0.0043}$ and the slope of the power law mass profile to be $\gamma = 2.0540^{+0.0553}_{-0.0714}$. The total mass within the critical curve is $8.312^{+0.108}_{-0.062} \times 10^{11} M_{\odot}$. The magnification results using the three methods in the Appendix of Paper I are shown in Table 4. The uncertainties for the magnification values of image B are the largest due to its proximity to the critical curve.

Table 4. Magnification estimates for DESI J234.4783+14.7232 using three methods. Values are shown for images A through D.

| Method | A | B | C | D | Total |
|-----------------|----------------|----------------|-----------------|-----------------|----------------|
| 1 st | 19.8 ± 2.2 | 38.5 ± 8.2 | 7.13 ± 0.22 | 0.49 ± 0.22 | 67.6 ± 8.5 |
| 2 nd | 17.3 ± 1.3 | 28.7 ± 5.2 | 8.14 ± 0.91 | 0.23 ± 0.15 | 54.6 ± 5.4 |
| 3 rd | 18.8 ± 2.0 | 34.7 ± 5.3 | 7.17 ± 0.49 | 0.49 ± 0.09 | 62.3 ± 5.7 |

4.2. DESI J238.5690+04.7276

DESI J238.5690+04.7276 was discovered in H21, with a ResNet probability of 1.00, and a human score of 2.5 (out of 4.0), corresponding to a C grade. As stated in H21, all candidates with a human inspection score ≥ 2.5 are likely lensing systems. The lens redshift, $z_d = 0.7768$ is from DESI DR1 (based on the 4000 Å break, Ca H&K absorption). The source redshift, $z_s = 1.72$ is from Keck NIRES (Paper VI, in prep.).

This system has an Einstein radius of $\theta_E = 1.5''$, slightly larger than the θ_E values of the simulated systems in the original GIGA-Lens paper (1.1''). Due to its relatively small size in the set of systems modeled in this work, uncluttered environment (Figure 6), it is relatively straightforward to model. We use a cutout with 120×120 pixels and a 27×27 pixel empirical PSF, generated using the procedure outlined in Section A.

We model the lens light with two elliptical Sérsic profiles. We mask out two small objects, one to the northwest (upper right) and another near a lensed arc (circles in Figure 6). We model the source using two elliptical Sérsic profiles. In addition, we model the light but not mass of an environmental galaxy to the southeast with an elliptical Sérsic profile (arrow in Figure 6), for a total of 38 parameters.

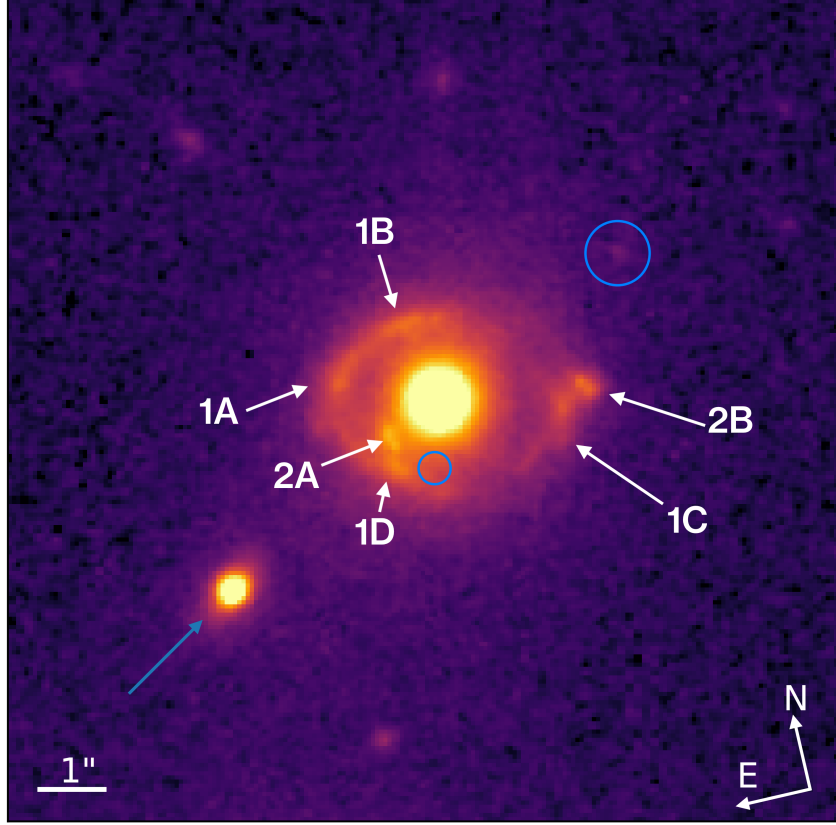


Figure 6. DESI J238.5690+04.7276. We mask out pixels in the two circles, and model the light of the environmental galaxy in the lower left (blue arrow). The two sources are lensed into a quad (images labeled 1A, 1B, 1C, and 1D) and a double (2A and 2B).

This system is modeled with linear inversion to solve for the light intensities. We achieved a reduced $\chi^2 = 0.95$ with superb residuals (Figure 7). The best-fit lens and external shear parameters are presented in Table 5 and their sampling results are shown in Figure 8. The best-fit light parameters are presented in Table 6.

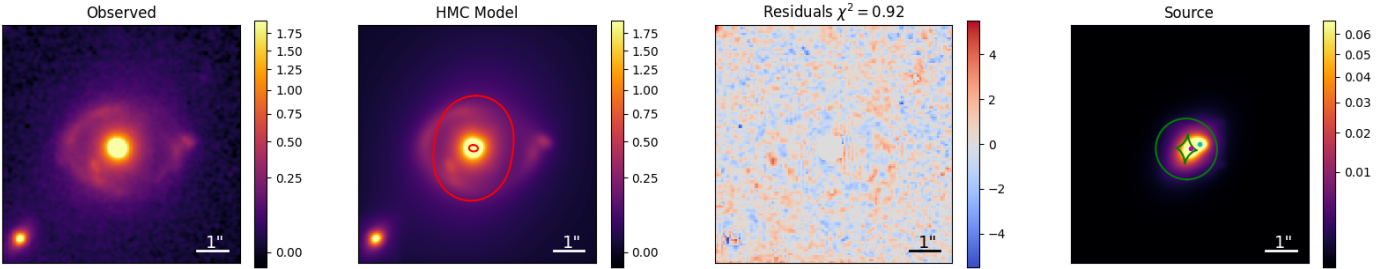


Figure 7. Best-fit Model DESI J238.5690+04.7276. From left to right, we show: the observed Hubble image, our best-fit model with the critical curve, the reduced residuals, and the unlensed source with the caustic. For calculating χ^2 we mask a circular region with a width of 12 pixels ($0.8''$) at the center of the lensing galaxy. This area is not masked during modeling. The unmasked χ^2 is 1.004. Only the two circles in Figure 6 are masked during modeling.

Table 5. Best-fit mass parameters for DESI J238.5690+04.7276.

| θ_E | γ | ϵ_1 | ϵ_2 | x | y | $\gamma_{ext,1}$ | $\gamma_{ext,2}$ |
|---------------------------|-----------------|-------------------|---------------------------|--------------------|--------------------|--------------------|--------------------|
| $1.475^{+0.002}_{-0.003}$ | 1.89 ± 0.02 | 0.037 ± 0.006 | $0.011^{+0.005}_{-0.006}$ | -0.123 ± 0.003 | -0.139 ± 0.003 | -0.161 ± 0.004 | -0.024 ± 0.004 |

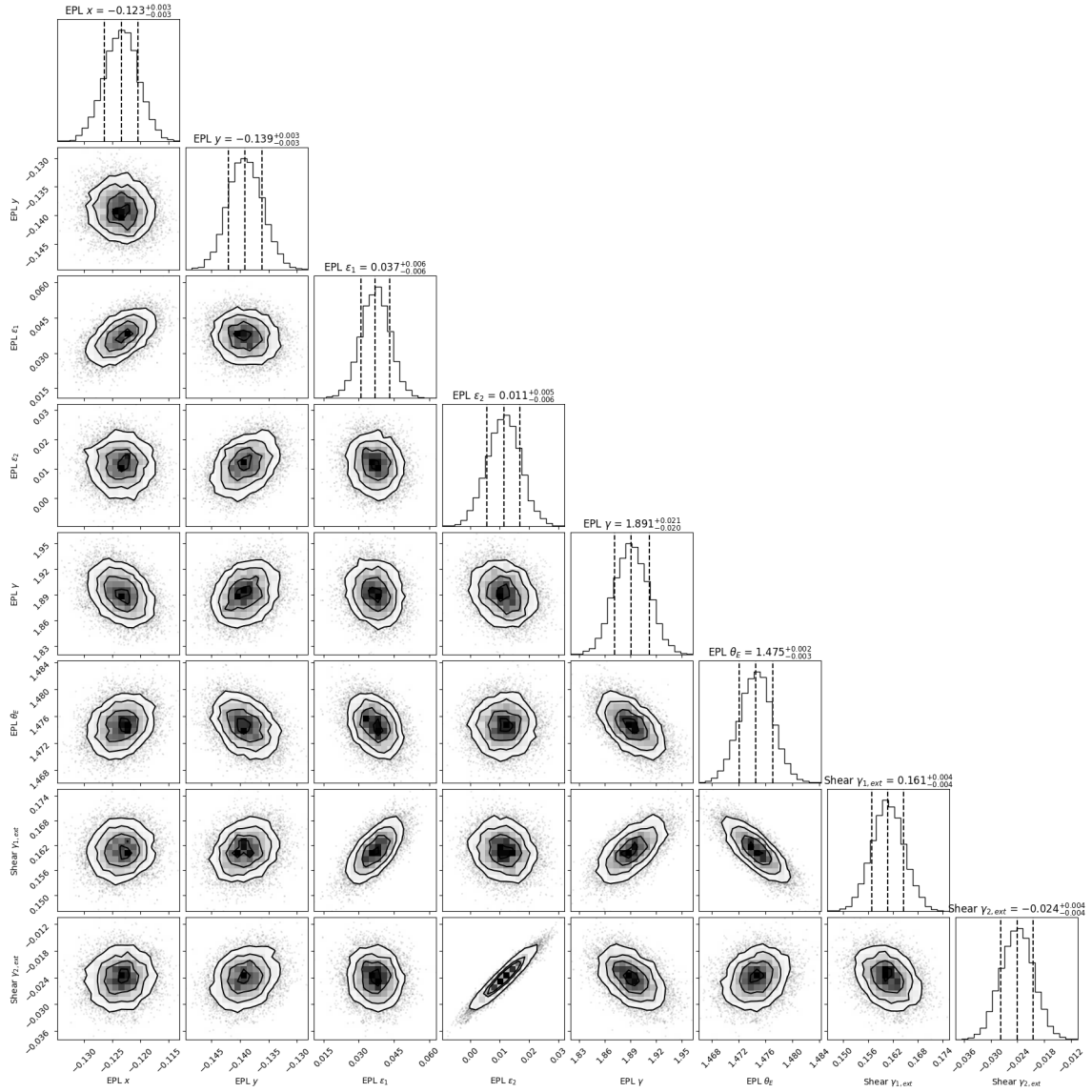
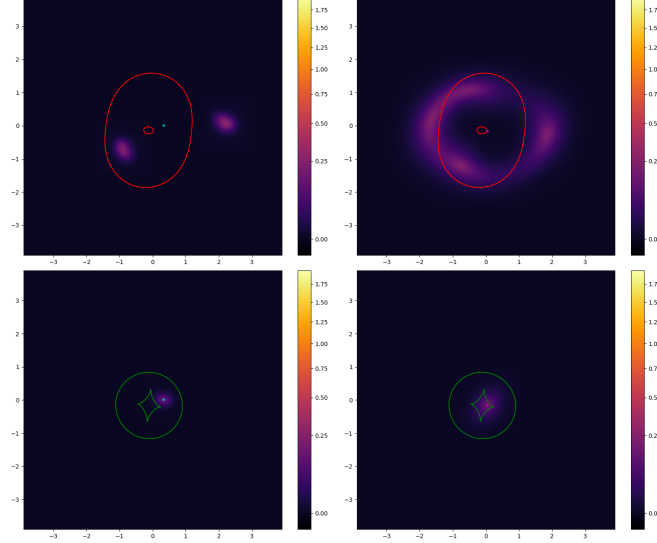
**Figure 8.** Corner plot of the eight mass parameters for DESI J238.5690+04.7276.

Table 6. Best-fit light parameters for DESI J238.5690+04.7276

| Parameter | Lens | | Source | | Environmental galaxy |
|--------------|-------------------------------|---------------------------|------------------------|--------------------|---------------------------|
| | Comp 1 | Comp 2 | Comp 1 | Comp 2 | |
| R_e | $0.452^{+0.007}_{-0.006}$ | 0.63 ± 0.01 | 0.072 ± 0.002 | 0.247 ± 0.007 | 0.058 ± 0.002 |
| n | $2.375^{+0.09}_{-0.06}$ | $3.884^{+0.05}_{-0.06}$ | $0.31^{+0.07}_{-0.05}$ | 1.18 ± 0.04 | $9.95^{+0.04}_{-0.08}$ |
| ϵ_1 | -0.122 ± 0.006 | -0.095 ± 0.003 | 0.30 ± 0.02 | -0.053 ± 0.009 | -0.133 ± 0.006 |
| ϵ_2 | 0.147 ± 0.005 | $0.103^{+0.003}_{-0.002}$ | -0.06 ± 0.02 | 0.207 ± 0.008 | $0.289^{+0.005}_{-0.006}$ |
| x | -0.0975 ± 0.0003 | -0.108 ± 0.001 | 0.33 ± 0.01 | 0.042 ± 0.003 | -3.3155 ± 0.0004 |
| y | $-0.0330^{+0.0004}_{-0.0010}$ | -0.067 ± 0.002 | 0.013 ± 0.005 | -0.151 ± 0.003 | -3.0873 ± 0.0006 |

We show the two Sérsic components for the source in (Figure 9). One source (component 1) is lensed into a double, while the other (component 2) is lensed into an Einstein cross. The redshift for component 2 is $z_s = 1.7210$. Component 1 was targeted by DESI and Keck NIRES; however, so far we have not detected any clear spectral features. Given the proximity of the unlensed positions of these two components, they possibly indicate a source with two components or a pair of merging galaxies.


Figure 9. From left to right, source component 1 and 2, respectively, in the lensed and unlensed plane for DESI J238.5690+04.7276.

For MAP, we used $n_{\text{MAP}} = 4000$ samples over 1000 steps, with square root transition over all 1000 iterations from an initial learning rate of -1×10^{-2} to a final value of -1×10^{-4} . It ran for five minutes and 55 seconds. For SVI, we used $n_{\text{VI}} = 500$ samples over 6000 iterations, with a square root transition from an initial learning rate of 1×10^{-6} to a final value of 1×10^{-3} . This stage lasted

10 minutes. Finally, for HMC we employed 16 chains over 160,000 steps, sampling every 100 steps for a total of 1,200 samples per chain after the 400 sample burn-in. We also discard the first half of the samples and only use the latter 600/chain for reporting the posterior distribution. The target acceptance probability was set at 0.75, with an initial step size of $\epsilon = 0.03$, $L = 3$ initial leapfrog steps, and a maximum of 30 leapfrog steps. HMC ran for 193 minutes and 36 seconds. The total execution time for all three modeling steps was 209 minutes and 31 seconds. We have successfully sampled this system with \hat{R} values below 1.1 for all parameters.

The best-fit Einstein radius $\theta_E = 1.475''_{-0.003}^{+0.002}$ and the mass profile slope, $\gamma = 1.89 \pm 0.02$. The total projected mass within the critical curve is $9.91 \pm 0.04 \times 10^{11} M_{\odot}$. For magnifications, we use three different methods as described in the Appendix of Paper I. The results are shown in Table 7.

Table 7. Magnifications for DESI J238.5690+04.7276 using three methods. We drew 250 random samples from the HMC chains for the calculation.

| Method | 1A | 1B | 1C | 1D | Total 1 | 2A | 2B | Total 2 |
|-----------------|---------------|----------------|---------------|----------------|----------------|----------------|---------------|---------------|
| 1 st | 8.4 ± 0.4 | -5.9 ± 0.4 | 3.7 ± 0.1 | -3.9 ± 0.2 | 22.0 ± 1.1 | -2.4 ± 0.1 | 2.9 ± 0.1 | 5.3 ± 0.2 |
| 2 nd | 8.5 ± 0.4 | -6.0 ± 0.4 | 3.8 ± 0.2 | -4.1 ± 0.2 | 22.5 ± 1.1 | -2.5 ± 0.1 | 2.9 ± 0.1 | 5.4 ± 0.2 |
| 3 rd | 8.1 ± 0.4 | -5.8 ± 0.3 | 3.7 ± 0.1 | -3.9 ± 0.2 | 21.5 ± 1.0 | -2.4 ± 0.1 | 2.9 ± 0.1 | 5.3 ± 0.2 |

5. DISCUSSION

5.1. Full Forward Modeling and Convergence Metrics

In this work, we have achieved two main goals: 1) full forward modeling for all six systems—all parameters describing the lens and the source are sampled simultaneously in a single inference. 2) All six systems meet explicit, quantitative criteria for statistical convergence based on both the Gelman–Rubin statistic (\hat{R}) and effective sample size (ESS). This is despite the fact that the systems modeled in this work span a wide range of image morphology, Einstein radii, and environmental complexity (Table 1). Together with the system in Paper I, this brings the total to seven.

This demonstrates that fully Bayesian modeling of complex, bright, galaxy-scale lenses with high-resolution space-based imaging can yield robust inferences, even for highly nonlinear strong-lensing models with $\gtrsim 40$ parameters determined *simultaneously*. These results underscore the steadily increasing maturity of strong gravitational lens modeling and provide a foundation for exploiting the thousands of high-quality lenses with high resolution soon to arrive from *HST*, *Euclid*, *Roman*, and *JWST* (e.g., Nightingale et al. 2025; Silver et al. 2025).

This approach stands in contrast to “staged” modeling strategies (e.g., optimize lens light first, then fix those parameters before optimizing mass, and so on). While computationally convenient, such sequential procedures have two major drawbacks: 1) they effectively impose more restrictive priors and risk converging to a local rather than global optimum, where the posterior probability mass is the greatest; and 2) they can artificially suppress the posterior variance of key quantities such as the mass density slope, γ . By jointly modeling and sampling *all* parameters pertaining to the lens mass, lens and source light, and external shear, our posterior space is not constrained by the order in which individual components are optimized.

5.2. Incorporation of Environmental Galaxies in Full Forward Modeling

We have, in fact, gone beyond simultaneously modeling the lens and source parameters in this work. For two systems in this sample—DESI J165.6876-06.0423 and DESI J238.5690+04.7276—we also include the light of the environmental galaxies directly in the full forward modeling. DESI J257.4348+31.9046 does not have an environmental galaxy bright enough to be modeled. For each of the remaining four systems, we fix only five or six light profile parameters associated with a single environmental galaxy, except in the most complex case, DESI J246.0062+01.4836 (§ B.5), which has 78 parameters in total. For this system, 28 light profile parameters for three environmental galaxies are fixed for sampling tractability, while the 50 parameters pertaining to the lens and the source are sampled simultaneously—an unprecedented scale for a galaxy-scale lens using *HST*-quality imaging.

Our next step is to incorporate the environmental galaxies in these four systems into full forward modeling, then extend this approach to all 26 galaxy-scale lenses in our *HST* program (see Paper I), and ultimately to group- and cluster-scale lenses (e.g., Sheu et al. 2024).

5.3. Mass Slope Evolution

The predicted evolution of γ with redshift is subtle, and robust inference requires reliable characterization of the intrinsic scatter in these measurements. Published γ - z distributions, including the recent AGEL results of Sahu et al. (2024), reveal a tight locus of slopes near the isothermal value at $z_d \lesssim 0.3$, but a wider distribution at $0.5 \lesssim z_d \lesssim 0.8$. Our results reinforce this broader picture: lenses in

this redshift range span $\gamma = 1.4\text{--}2.5$, comparable to the full range seen in the literature. We also report the mass density slope for an elliptical galaxy at $z_d > 1$: $\gamma = 2.616 \pm 0.17$ for DESI J246.0062+01.4836 at $z_d = 1.092$.

5.4. Lens Modeling Time

Finally, we note that the modeling times quoted in this work reflect the time required to achieve convergence for all parameters sampled according to the \hat{R} and ESS criteria. If only “presentable” corner plots and reasonable residuals were desired, execution times would be an order of magnitude or more shorter. The timing benchmarks presented here should therefore be interpreted as practical estimates for rigorous, convergence-validated modeling.

Together, these advances establish a framework that can support a new generation of precision strong lensing studies. With validated posteriors, the data presented here—and especially larger samples to come—can confidently address high-impact questions in galaxy evolution and cosmology.

6. CONCLUSION

In this Paper V of the DESI Strong Lens Foundry series, we present the first sample of strong lenses with *HST* modeled with full forward modeling and quantitative convergence validation (\hat{R} and ESS). We use the open-source **GIGA-Lens**. For each of the seven systems in this sample, we achieve $\hat{R} < 1.1$ and ESS $> 10,000$ for every lens and source parameter and establish a methodological foundation for large-sample studies of galaxy-scale strong lenses. Reporting quantitative sampling-convergence diagnostics such as \hat{R} and ESS has become standard in cosmological inference, and strong-lensing analyses are now positioned to benefit from the same transparent practices.

In this sample, we observe increased scatter in γ at intermediate redshifts ($z \sim 0.5\text{--}0.8$), consistent with earlier reports. Our sample also extends mass density slope inference for elliptical galaxies beyond $z = 1$, with a convergence-validated measurement of $\gamma = 2.62 \pm 0.17$ for DESI J246.0062+01.4836 at $z_d = 1.092$. In our view, a more definitive conclusion on the mass slope evolution awaits a uniform, convergence-tested, and full forward modeling effort across a large sample of systems—including the known lenses—so that statistical uncertainties are robustly characterized and intrinsic redshift evolution can then be distinguished from modeling systematics and galaxy-to-galaxy diversity.

Modeling real systems with high-resolution data is inherently more challenging than fitting simulated systems (Gu22), as we previously demonstrated in our application of **GIGA-Lens** to *HST* observations (Huang et al. 2025a, Paper I). The present analysis further shows that large θ_E , complex environments, and source light structure can significantly increase the cutout size and number of model parameters, making efficient sampling more challenging. We nevertheless confirm that with **GIGA-Lens**, as in Paper I, convergence-validated, full forward modeling is scalable to the dimensionality required by real systems. Continued improvements in GPU-parallel inference and adaptive covariance learning (N. Ratier-Werbin et al. in prep.) will further expand feasibility to much larger lens samples. With continued hardware and software advances in GPU-accelerated modeling and flexible parameterizations, strong lensing is poised to deliver precision constraints on galaxy evolution, dark matter physics, and cosmology in the era of thousands, if not tens of thousands, of high-quality strong lenses.

ACKNOWLEDGMENT

We thank Peter Harrington, Nestor Demeure, Steve Farrell, and Rollin Thomas at the National Energy Scientific Computing Center (NERSC) for their consultation and advice. This research used resources of the National Energy Research Scientific Computing Center (NERSC), a U.S. Department of Energy Office of Science User Facility operated under Contract No. DE-AC02-05CH11231 and the Computational HEP program in The Department of Energy’s Science Office of High Energy Physics provided resources through the “Cosmology Data Repository” project (Grant #KA2401022). X.H. acknowledges the University of San Francisco Faculty Development Fund. A.D.’s research is supported by National Science Foundation’s National Optical-Infrared Astronomy Research Laboratory, which is operated by the Association of Universities for Research in Astronomy (AURA) under cooperative agreement with the National Science Foundation.

This paper is based on observations at Cerro Tololo Inter-American Observatory, National Optical Astronomy Observatory (NOAO Prop. ID: 2014B-0404; co-PIs: D. J. Schlegel and A. Dey), which is operated by the Association of Universities for Research in Astronomy (AURA) under a cooperative agreement with the National Science Foundation.

This project used data obtained with the Dark Energy Camera (DECam), which was constructed by the Dark Energy Survey (DES) collaboration. Funding for the DES Projects has been provided by the U.S. Department of Energy, the U.S. National Science Foundation, the Ministry of Science and Education of Spain, the Science and Technology Facilities Council of the United Kingdom, the Higher Education Funding Council for England, the National Center for Supercomputing Applications at the University of Illinois at Urbana-Champaign, the Kavli Institute of Cosmological Physics at the University of Chicago, the Center for Cosmology and Astro-Particle Physics at the Ohio State University, the Mitchell Institute for Fundamental Physics and Astronomy at Texas A&M University, Financiadora de Estudos e Projetos, Fundação Carlos Chagas Filho de Amparo à Pesquisa do Estado do Rio de Janeiro, Conselho Nacional de Desenvolvimento Científico e Tecnológico and the Ministério da Ciência, Tecnologia e Inovação, the Deutsche Forschungsgemeinschaft, and the Collaborating Institutions in the Dark Energy Survey. The Collaborating Institutions are Argonne National Laboratory, the University of California at Santa Cruz, the University of Cambridge, Centro de Investigaciones Energéticas, Medioambientales y Tecnológicas-Madrid, the University of Chicago, University College London, the DES-Brazil Consortium, the University of Edinburgh, the Eidgenössische Technische Hochschule (ETH) Zürich, Fermi National Accelerator Laboratory, the University of Illinois at Urbana-Champaign, the Institut de Ciències de l’Espai (IEEC/CSIC), the Institut de Física d’Altes Energies, Lawrence Berkeley National Laboratory, the Ludwig-Maximilians Universität München and the associated Excellence Cluster Universe, the University of Michigan, the National Optical Astronomy Observatory, the University of Nottingham, the Ohio State University, the OzDES Membership Consortium the University of Pennsylvania, the University of Portsmouth, SLAC National Accelerator Laboratory, Stanford University, the University of Sussex, and Texas A&M University.

Software: TensorFlow (Abadi et al. 2015), TensorFlow Probability (Dillon et al. 2017), JAX (Bradbury et al. 2018), Optax (Hessel et al. 2020), lenstronomy (Birrer & Amara 2018), Matplotlib

(Hunter 2007), photutils (Bradley et al. 2023) seaborn (Waskom 2021), corner.py (Foreman-Mackey 2016), NumPy (Harris et al. 2020)

REFERENCES

- Abadi, M., Agarwal, A., Barham, P., et al. 2015, TensorFlow: Large-Scale Machine Learning on Heterogeneous Systems. <https://www.tensorflow.org/>
- Abbott, B. P., Abbott, R., Abbott, T. D., et al. 2017, *Nature*, 551, 85, doi: [10.1038/nature24471](https://doi.org/10.1038/nature24471)
- Abbott, T. M. C., Abdalla, F. B., Annis, J., et al. 2018, *MNRAS*, 480, 3879, doi: [10.1093/mnras/sty1939](https://doi.org/10.1093/mnras/sty1939)
- Agarwal, S., Huang, X., Sheu, W., et al. 2025, arXiv e-prints, arXiv:2509.18086, doi: [10.48550/arXiv.2509.18086](https://doi.org/10.48550/arXiv.2509.18086)
- Ahumada, R., Allende Prieto, C., Almeida, A., et al. 2020, *ApJS*, 249, 3, doi: [10.3847/1538-4365/ab929e](https://doi.org/10.3847/1538-4365/ab929e)
- Birrer, S., & Amara, A. 2018, *Physics of the Dark Universe*, 22, 189, doi: [10.1016/j.dark.2018.11.002](https://doi.org/10.1016/j.dark.2018.11.002)
- Birrer, S., Amara, A., & Refregier, A. 2015, *ApJ*, 813, 102, doi: [10.1088/0004-637X/813/2/102](https://doi.org/10.1088/0004-637X/813/2/102)
- Blandford, R. D., & Narayan, R. 1992, *ARA&A*, 30, 311, doi: [10.1146/annurev.astro.30.1.311](https://doi.org/10.1146/annurev.astro.30.1.311)
- Bolton, A. S., Burles, S., Koopmans, L. V. E., Treu, T., & Moustakas, L. A. 2006, *ApJ*, 638, 703, doi: [10.1086/498884](https://doi.org/10.1086/498884)
- Bolton, A. S., Brownstein, J. R., Kochanek, C. S., et al. 2012, *ApJ*, 757, 82, doi: [10.1088/0004-637X/757/1/82](https://doi.org/10.1088/0004-637X/757/1/82)
- Brada, M., Allen, S. W., Treu, T., et al. 2008, *ApJ*, 687, 959967, doi: [10.1086/591246](https://doi.org/10.1086/591246)
- Bradbury, J., Frostig, R., Hawkins, P., et al. 2018, JAX: composable transformations of Python+NumPy programs. <http://github.com/google/jax>
- Bradley, L., Sipőcz, B., Robitaille, T., et al. 2023, *astropy/photutils: 1.8.0*, Zenodo, doi: [10.5281/zenodo.7946442](https://doi.org/10.5281/zenodo.7946442)
- Broadhurst, T., Huang, X., Frye, B., & Ellis, R. 2000, *ApJL*, 534, L15, doi: [10.1086/312651](https://doi.org/10.1086/312651)
- Brooks, S. P., & Gelman, A. 1998, *Journal of Computational and Graphical Statistics*, 7, 434, doi: [10.1080/10618600.1998.10474787](https://doi.org/10.1080/10618600.1998.10474787)
- Çağan Şengül, A. Ç., Dvorkin, C., Ostdiek, B., & Tsang, A. 2022, *MNRAS*, 515, 4391, doi: [10.1093/mnras/stac1967](https://doi.org/10.1093/mnras/stac1967)
- Choi, S. K., Hasselfield, M., Ho, S.-P. P., et al. 2020, arXiv e-prints, arXiv:2007.07289
- Cikota, A., Bertolla, I. T., Huang, X., et al. 2023, *ApJL*, 953, L5, doi: [10.3847/2041-8213/ace9da](https://doi.org/10.3847/2041-8213/ace9da)
- Collett, T. E., & Auger, M. W. 2014, *MNRAS*, 443, 969, doi: [10.1093/mnras/stu1190](https://doi.org/10.1093/mnras/stu1190)
- Collett, T. E., Oldham, L. J., Smith, R. J., et al. 2018, *Science*, 360, 1342, doi: [10.1126/science.aao2469](https://doi.org/10.1126/science.aao2469)
- Dawes, C., Storfer, C., Huang, X., et al. 2023, *The Astrophysical Journal Supplement Series*, 269, 61, doi: [10.3847/1538-4365/ad015a](https://doi.org/10.3847/1538-4365/ad015a)
- DESI Collaboration, Abdul-Karim, M., Adame, A. G., et al. 2025, arXiv e-prints, arXiv:2503.14745, doi: [10.48550/arXiv.2503.14745](https://doi.org/10.48550/arXiv.2503.14745)
- Dey, A., Schlegel, D. J., Lang, D., et al. 2019, *AJ*, 157, 168, doi: [10.3847/1538-3881/ab089d](https://doi.org/10.3847/1538-3881/ab089d)
- Dhawan, S., Thorp, S., Mandel, K. S., et al. 2023, *MNRAS*, 524, 235, doi: [10.1093/mnras/stad1590](https://doi.org/10.1093/mnras/stad1590)
- Diaz Rivero, A., & Dvorkin, C. 2020, *PhRvD*, 101, 023515, doi: [10.1103/PhysRevD.101.023515](https://doi.org/10.1103/PhysRevD.101.023515)
- Dillon, J. V., Langmore, I., Tran, D., et al. 2017, TensorFlow Distributions
- Filipp, A., Shu, Y., Pakmor, R., Suyu, S. H., & Huang, X. 2023, *A&A*, 677, A113, doi: [10.1051/0004-6361/202346594](https://doi.org/10.1051/0004-6361/202346594)
- Foreman-Mackey, D. 2016, *The Journal of Open Source Software*, 1, 24, doi: [10.21105/joss.00024](https://doi.org/10.21105/joss.00024)
- Freedman, W. L., Madore, B. F., Hatt, D., et al. 2019, *ApJ*, 882, 34, doi: [10.3847/1538-4357/ab2f73](https://doi.org/10.3847/1538-4357/ab2f73)
- Freedman, W. L., Madore, B. F., Hoyt, T., et al. 2020, *ApJ*, 891, 57, doi: [10.3847/1538-4357/ab7339](https://doi.org/10.3847/1538-4357/ab7339)
- Gelman, A., Carlin, J. B., Stern, H. S., et al. 2014, *Bayesian Data Analysis*
- Gelman, A., & Rubin, D. B. 1992, *Statistical Science*, 7, 457, doi: [10.1214/ss/1177011136](https://doi.org/10.1214/ss/1177011136)
- Gu, A., Huang, X., Sheu, W., et al. 2022, *ApJ*, 935, 49, doi: [10.3847/1538-4357/ac6de4](https://doi.org/10.3847/1538-4357/ac6de4)

- Harris, C. R., Millman, K. J., van der Walt, S. J., et al. 2020, *Nature*, 585, 357, doi: [10.1038/s41586-020-2649-2](https://doi.org/10.1038/s41586-020-2649-2)
- Hessel, M., Budden, D., Viola, F., et al. 2020, Optax: composable gradient transformation and optimisation, in JAX! <http://github.com/deepmind/optax>
- Hezaveh, Y. D., Dalal, N., Marrone, D. P., et al. 2016, *ApJ*, 823, 37, doi: [10.3847/0004-637X/823/1/37](https://doi.org/10.3847/0004-637X/823/1/37)
- Hsu, Y.-M., Huang, X., Storfer, C. J., et al. 2025, arXiv e-prints, arXiv:2509.16033, doi: [10.48550/arXiv.2509.16033](https://doi.org/10.48550/arXiv.2509.16033)
- Huang, X., Morokuma, T., Fakhouri, H. K., et al. 2009, *ApJ*, 707, L12, doi: [10.1088/0004-637X/707/1/L12](https://doi.org/10.1088/0004-637X/707/1/L12)
- Huang, X., Storfer, C., Ravi, V., et al. 2020, *The Astrophysical Journal*, 894, 78, doi: [10.3847/1538-4357/ab7ffb](https://doi.org/10.3847/1538-4357/ab7ffb)
- Huang, X., Storfer, C., Gu, A., et al. 2021, *ApJ*, 909, 27, doi: [10.3847/1538-4357/abd62b](https://doi.org/10.3847/1538-4357/abd62b)
- Huang, X., Baltasar, S., Ratier-Werbin, N., et al. 2025a, <https://arxiv.org/abs/2502.03455>
- Huang, X., Inchausti, J. C., Storfer, C. J., et al. 2025b, arXiv e-prints, arXiv:2509.18089, doi: [10.48550/arXiv.2509.18089](https://doi.org/10.48550/arXiv.2509.18089)
- Hunter, J. D. 2007, *Computing in Science & Engineering*, 9, 90, doi: [10.1109/MCSE.2007.55](https://doi.org/10.1109/MCSE.2007.55)
- Inchausti, J. C., Storfer, C. J., Huang, X., et al. 2025, arXiv e-prints, arXiv:2508.20087, doi: [10.48550/arXiv.2508.20087](https://doi.org/10.48550/arXiv.2508.20087)
- Jauzac, M., Harvey, D., & Massey, R. 2018, *MNRAS*, 477, 4046, doi: [10.1093/mnras/sty909](https://doi.org/10.1093/mnras/sty909)
- Jullo, E., Natarajan, P., Kneib, J. P., et al. 2010, *Science*, 329, 924, doi: [10.1126/science.1185759](https://doi.org/10.1126/science.1185759)
- Karp, J. S. M., Schlegel, D. J., Huang, X., et al. 2025, arXiv e-prints, arXiv:2512.04275, doi: [10.48550/arXiv.2512.04275](https://doi.org/10.48550/arXiv.2512.04275)
- Kelly, P. L., Rodney, S., Treu, T., et al. 2023, *ApJ*, 948, 93, doi: [10.3847/1538-4357/ac4ccb](https://doi.org/10.3847/1538-4357/ac4ccb)
- Khetan, N., Izzo, L., Branchesi, M., et al. 2020, arXiv e-prints, arXiv:2008.07754
- Kochanek, C. S. 1991, *ApJ*, 373, 354, doi: [10.1086/170057](https://doi.org/10.1086/170057)
- Koopmans, L. V. E., & Treu, T. 2002, *ApJL*, 568, L5, doi: [10.1086/340143](https://doi.org/10.1086/340143)
- Koopmans, L. V. E., Treu, T., Bolton, A. S., Burles, S., & Moustakas, L. A. 2006, *ApJ*, 649, 599, doi: [10.1086/505696](https://doi.org/10.1086/505696)
- Limousin, M., Cabanac, R., Gavazzi, R., et al. 2009, *A&A*, 502, 445, doi: [10.1051/0004-6361/200811473](https://doi.org/10.1051/0004-6361/200811473)
- Lin, E., Toro Bertolla, I., Cikota, A., et al. 2025, arXiv e-prints, arXiv:2509.18078, doi: [10.48550/arXiv.2509.18078](https://doi.org/10.48550/arXiv.2509.18078)
- Linder, E. V. 2011, *PhRvD*, 84, 123529, doi: [10.1103/PhysRevD.84.123529](https://doi.org/10.1103/PhysRevD.84.123529)
- Mandel, K. S., Thorp, S., Narayan, G., Friedman, A. S., & Avelino, A. 2022, *MNRAS*, 510, 3939, doi: [10.1093/mnras/stab3496](https://doi.org/10.1093/mnras/stab3496)
- Meneghetti, M., Davoli, G., Bergamini, P., et al. 2020, *Science*, 369, 1347, doi: [10.1126/science.aax5164](https://doi.org/10.1126/science.aax5164)
- Nierenberg, A. M., Keeley, R. E., Sluse, D., et al. 2023, arXiv e-prints, arXiv:2309.10101, doi: [10.48550/arXiv.2309.10101](https://doi.org/10.48550/arXiv.2309.10101)
- Nightingale, J. W., Mahler, G., McCleary, J., et al. 2025, *MNRAS*, 543, 203, doi: [10.1093/mnras/staf1253](https://doi.org/10.1093/mnras/staf1253)
- O'Donnell, J. H., Jeltema, T. E., Roberts, M. G., et al. 2025, arXiv e-prints, arXiv:2508.20179, doi: [10.48550/arXiv.2508.20179](https://doi.org/10.48550/arXiv.2508.20179)
- Oguri, M., & Marshall, P. J. 2010, *MNRAS*, 405, 2579, doi: [10.1111/j.1365-2966.2010.16639.x](https://doi.org/10.1111/j.1365-2966.2010.16639.x)
- Pascale, M., Frye, B. L., Pierel, J. D. R., et al. 2025, *ApJ*, 979, 13, doi: [10.3847/1538-4357/ad9928](https://doi.org/10.3847/1538-4357/ad9928)
- Philcox, O. H. E., Sherwin, B. D., Farren, G. S., & Baxter, E. J. 2020, arXiv e-prints, arXiv:2008.08084
- Pierel, J. D. R., Rodney, S., Vernardos, G., et al. 2021, *ApJ*, 908, 190, doi: [10.3847/1538-4357/abd8d3](https://doi.org/10.3847/1538-4357/abd8d3)
- Planck Collaboration, Aghanim, N., Akrami, Y., et al. 2020, *A&A*, 641, A6, doi: [10.1051/0004-6361/201833910](https://doi.org/10.1051/0004-6361/201833910)
- Refsdal, S. 1964, *MNRAS*, 128, 307, doi: [10.1093/mnras/128.4.307](https://doi.org/10.1093/mnras/128.4.307)
- Riess, A. G., Casertano, S., Yuan, W., Macri, L. M., & Scolnic, D. 2019, *ApJ*, 876, 85, doi: [10.3847/1538-4357/ab1422](https://doi.org/10.3847/1538-4357/ab1422)
- Ritondale, E., Vegetti, S., Despali, G., et al. 2019, *MNRAS*, 485, 2179, doi: [10.1093/mnras/stz464](https://doi.org/10.1093/mnras/stz464)
- Sahu, N., Tran, K.-V., Suyu, S. H., et al. 2024, *ApJ*, 970, 86, doi: [10.3847/1538-4357/ad4ce3](https://doi.org/10.3847/1538-4357/ad4ce3)
- Shajib, A. J., Treu, T., Birrer, S., & Sonnenfeld, A. 2020, arXiv e-prints, arXiv:2008.11724, <https://arxiv.org/abs/2008.11724>

- Shajib, A. J., Birrer, S., Treu, T., et al. 2019, *MNRAS*, 483, 5649, doi: [10.1093/mnras/sty3397](https://doi.org/10.1093/mnras/sty3397)
- Sharma, D., Collett, T. E., & Linder, E. V. 2023, *JCAP*, 2023, 001, doi: [10.1088/1475-7516/2023/04/001](https://doi.org/10.1088/1475-7516/2023/04/001)
- Sharma, D., & Linder, E. V. 2022, arXiv e-prints, arXiv:2204.03020
- Sheu, W., Cikota, A., Huang, X., et al. 2024, *ApJ*, 973, 3, doi: [10.3847/1538-4357/ad65d3](https://doi.org/10.3847/1538-4357/ad65d3)
- Silver, E., Wang, R., Huang, X., et al. 2025, *ApJ*, 994, 117, doi: [10.3847/1538-4357/adf3b0](https://doi.org/10.3847/1538-4357/adf3b0)
- Storfer, C., Huang, X., Gu, A., et al. 2024, *ApJS*, 274, 16, doi: [10.3847/1538-4365/ad527e](https://doi.org/10.3847/1538-4365/ad527e)
- Suyu, S. H., Goobar, A., Collett, T., More, A., & Vernardos, G. 2023, arXiv e-prints, arXiv:2301.07729, doi: [10.48550/arXiv.2301.07729](https://doi.org/10.48550/arXiv.2301.07729)
- Tamm, A., & Tenjes, P. 2006, *A&A*, 449, 67, doi: [10.1051/0004-6361:20054065](https://doi.org/10.1051/0004-6361:20054065)
- Tessore, N., Bellagamba, F., & Metcalf, R. B. 2016, *MNRAS*, 463, 3115, doi: [10.1093/mnras/stw2212](https://doi.org/10.1093/mnras/stw2212)
- The Dark Energy Survey Collaboration. 2005, arXiv e-prints, astro
- Treu, T. 2010, *ARA&A*, 48, 87, doi: [10.1146/annurev-astro-081309-130924](https://doi.org/10.1146/annurev-astro-081309-130924)
- Treu, T., & Marshall, P. J. 2016, *Astronomy and Astrophysics Review*, 24, 11, doi: [10.1007/s00159-016-0096-8](https://doi.org/10.1007/s00159-016-0096-8)
- Urcelay, F., Jullo, E., Barrientos, L. F., Huang, X., & Hernandez, J. 2025, *A&A*, 694, A35, doi: [10.1051/0004-6361/202449261](https://doi.org/10.1051/0004-6361/202449261)
- Vegetti, S., Despali, G., Lovell, M. R., & Enzi, W. 2018, *MNRAS*, 481, 3661, doi: [10.1093/mnras/sty2393](https://doi.org/10.1093/mnras/sty2393)
- Vegetti, S., & Koopmans, L. V. E. 2009, *MNRAS*, 400, 1583, doi: [10.1111/j.1365-2966.2009.15559.x](https://doi.org/10.1111/j.1365-2966.2009.15559.x)
- Vegetti, S., Koopmans, L. V. E., Auger, M. W., Treu, T., & Bolton, A. S. 2014, *MNRAS*, 442, 2017, doi: [10.1093/mnras/stu943](https://doi.org/10.1093/mnras/stu943)
- Verde, L., Treu, T., & Riess, A. G. 2019, *Nature Astronomy*, 3, 891, doi: [10.1038/s41550-019-0902-0](https://doi.org/10.1038/s41550-019-0902-0)
- Verdugo, T., Motta, V., Muñoz, R. P., et al. 2011, *A&A*, 527, A124, doi: [10.1051/0004-6361/201014965](https://doi.org/10.1051/0004-6361/201014965)
- Waskom, M. L. 2021, *Journal of Open Source Software*, 6, 3021, doi: [10.21105/joss.03021](https://doi.org/10.21105/joss.03021)
- Wong, K. C., Suyu, S. H., Chen, G. C. F., et al. 2019, arXiv e-prints, arXiv:1907.04869

APPENDIX

A. EFFECTIVE PSF GENERATION

This section describes the empirical point spread function (PSF) used for lens modeling. The PSF for each system is generated from stars extracted from the respective fits file containing the strong lensing system. We show the image containing DESI J154.6972-01.3590 as an example in figure 11. With the aim of selecting several stars in the *HST* image, we specify an appropriate pixel value threshold. Pixels belonging to other kinds of objects (e.g., galaxies) may be included in the list of brightest pixels. We therefore compare this list with the pixel positions in the image, and only keep the pixels that belong to stars. Moreover, we avoid very bright, saturated stars.

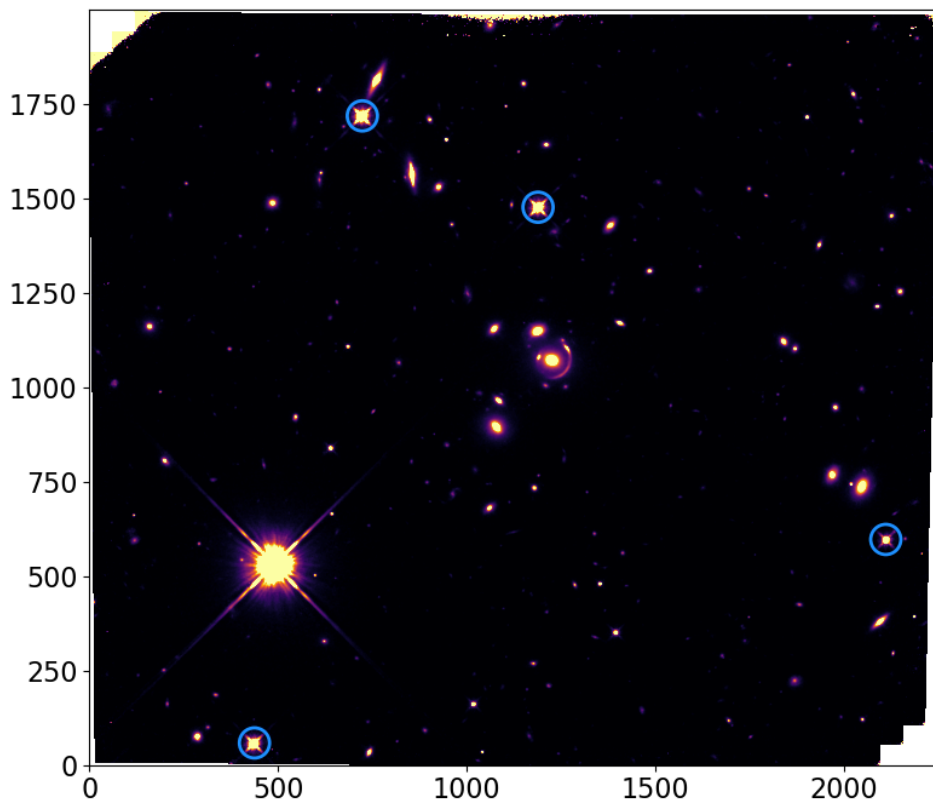


Figure 11. *HST* image containing DESI J154.6972-01.3590 (near the center of the image). Circled in blue are the four stars used to generate the empirical PSF.

Finally, the empirical PSF is generated from these cutouts using the `EPSFBuilder` function of `photutils`⁶. As an example, Figure 12 shows an empirical PSF for DESI J154.6972-01.3590.

⁶ <https://photutils.readthedocs.io/en/stable/>

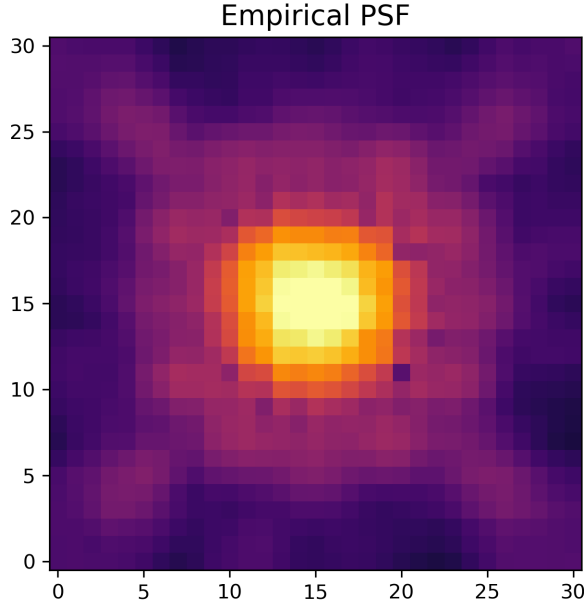


Figure 12. Empirical PSF for DESI J154.6972-01.3590, with 31 pixels on the side.

B. LENS MODELING RESULTS

Below we present the modeling results of DESI J154.6972-01.3590 (§ B.1), DESI J165.6876-06.0423 (modeled in Paper I, briefly summarized in § B.2), DESI J094.5639+50.3059 (§ B.3), DESI J257.4348+31.9046 (§ B.4), and DESI J246.0062+01.4836 (§ B.5), ordered by increasing lens redshift.

B.1. *DESI J154.6972-01.3590*

DESI J154.6972-01.3590 was discovered in H20, with a ResNet probability of 1.000, and a human grade of A. The lens redshift, $z_d = 0.3884$, is from SDSS DR16 (Ahumada et al. 2020) and DESI obtained its source redshift, $z_s = 1.4304$ with a strong [O II] detection.⁷

Figure 13 shows DESI J154.6972-01.3590. The Legacy Surveys image for this system features an elliptical galaxy as the lens. To its right, there is a long lensed arc with a bright “knot” near the top (denoted with the letter “A” in Figure 13). To the left of the lens is the counter image of the same lensed source, referred to by the letter “B”.

The cutout for this system has a size of 120×120 pixels. Besides the central elliptical galaxy and the lensed source, the cutout also contains other objects. There is a small environmental galaxy to the upper left of the main lensed arc (arrow in Figure 13). We include it as part of the lens model, and we will refer to it as the “nearby galaxy” (we only model its light). There are a few other even dimmer objects. The light and mass of these objects are not included in the lens model. They are masked out during the modeling process (circles in Figure 13). Finally, there is a bright object at about $5.5''$ from the lensing galaxy, to its upper left (also circled in Figure 13). DESI DR1 (DESI

⁷ There are actually two DESI spectra targeting the brightest knot of the main arc, yielding two slightly different redshifts at 1.4303 and 1.4305. This is within the redshift uncertainty of DESI (Paper II). In this work, we use the average of these two values, $z_s = 1.4304$.

Collaboration et al. 2025) reveals it to be a galaxy at $z = 0.7640$. It is far enough away that we do not model its mass and simply mask out its light.

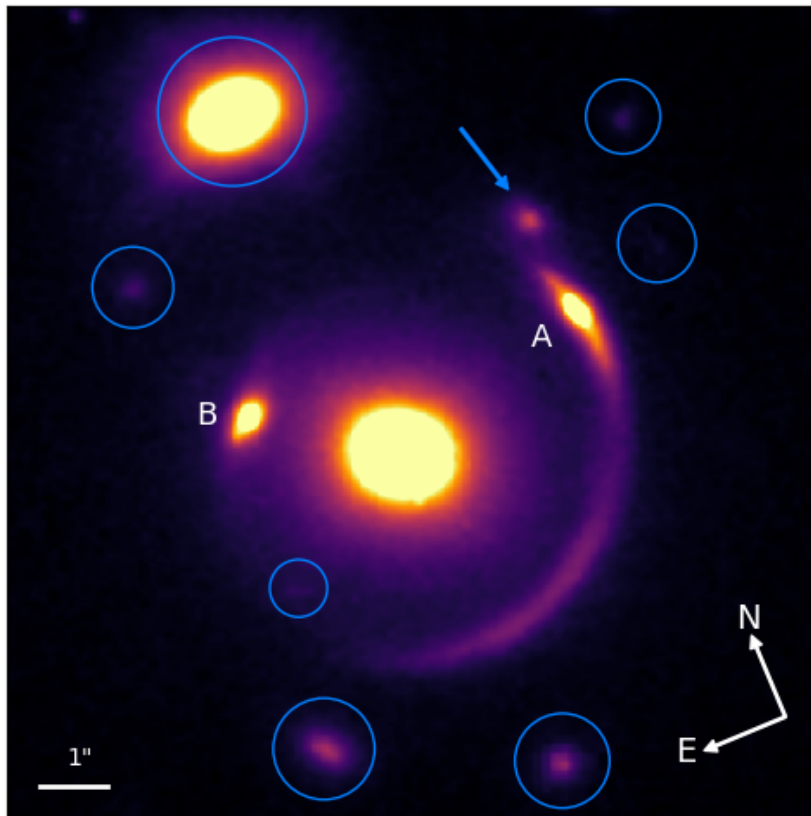


Figure 13. *HST* image of DESI J154.6972-01.3590. The brightest parts of the lensed images are labeled as A and B. Fainted objects circled in blue are masked and not modeled. We model the light of the small environmental galaxy (arrow) north of image A, and then fix its parameters (see text).

This is a challenging system to model, for three reasons. Firstly, its size. With an Einstein radius of nearly $\theta_E \sim 3''$, it stands at the limit between galaxy and group scale strong lensing (e.g., Limousin et al. 2009). For group/cluster lenses, the modeling is usually done only using the images positions and not at the pixel level (e.g., Verdugo et al. 2011). In addition, given that the area enclosed by θ_E is $\sim 9\times$ larger than typical galaxy-scale strong lens with a $\theta_E \sim 1''$, it is not a surprise that there are more environmental galaxies near the arcs. Each of these needs to be properly treated. Secondly, the lens is very bright. This is expected given that it is a massive lensing galaxy with a large θ_E . It is so luminous that faint diffraction spikes are visible out to $\sim 1.5''$ from the center of the lensing galaxy. Thus, we need to use a large PSF size of 59×59 pixels ($\sim 4\times$ larger than for the other systems in this work) to properly model its light at large radii. Thirdly, the lensed images are also very bright. In fact, their peak flux values are comparable to those of the lens; this is unusual. Typically, the lensed arcs are considerably fainter than the lens, which is certainly the case for the other systems in this work. But for this system, the signal to noise ratio (SNR) of the lensed images is very high. In fact, image B has an SNR around 250, and image A around 225, calculated by averaging flux value of the top 5% pixels. For comparison, the SNR's of the top 5% brightest pixels of the four images for DESI J234.4783+14.7232 (§ 4.1) range between 63.1 and 84.3. It is well known that source structure

can be difficult to model well. With a very high SNR for the “knots” in the lensed images in this system, this poses a significant challenge to lens modeling.

Our model consists of four elliptical Sérsic’s for the source light. For lens light, we mask the center of the lens and model it with a single elliptical Sérsic. Finally, for the nearby galaxy, we do not model its mass and its light is modeled by a single elliptical Sérsic profile. Initially, the six light parameters of this galaxy were modeled together with the rest of the model’s parameters. Once a good residual was achieved in that area, their values were fixed. This helps reduce the dimensionality of the model parameter space.

This system is modeled with linear inversion to solve for the light intensities. The final model after sampling from HMC is shown in Figure 14. The final reduced χ^2 is 0.786. The best-fit mass parameters for the lens appear in Table 8, and their posterior distribution in Figure 15. The best-fit values for the light parameters appear in Table 9.

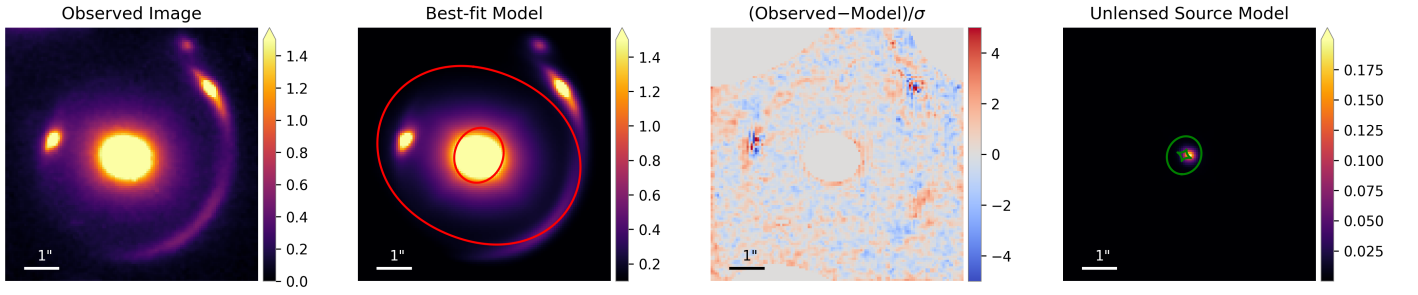


Figure 14. Our best-fit model. From left to right, we show: the observed *Hubble* image (the orientation is the same as in Figure 13), our best-fit model with critical curves. Note that since $\gamma < 2$, there are two critical curves and two caustics), the reduced residual, and the unlensed source with caustics.

Table 8. Best-fit mass parameters for DESI J154.6972-01.3590.

| θ_E | γ | ϵ_1 | ϵ_2 | x | y | $\gamma_{ext,1}$ | $\gamma_{ext,2}$ |
|------------------------------|-------------------|------------------------------|----------------------|-------------------------------|----------------------|-------------------------------|----------------------|
| $2.8982^{+0.0010}_{-0.0011}$ | 1.411 ± 0.016 | $0.0196^{+0.0022}_{-0.0020}$ | -0.0322 ± 0.0017 | $-0.1649^{+0.0033}_{-0.0035}$ | -0.0287 ± 0.0019 | $-0.0076^{+0.0024}_{-0.0022}$ | -0.0027 ± 0.0015 |

Table 9. Best-fit light parameters for DESI J154.6972-01.3590

| Parameter | Lens light | Source light | | | |
|--------------|---------------------------|-------------------------------|-------------------------------|-------------------------------|-------------------------------|
| | | Comp 1 | Comp 2 | Comp 3 | Comp 4 |
| R_e | $2.954^{+0.064}_{-0.062}$ | 0.0680 ± 0.0035 | $0.0533^{+0.0073}_{-0.0069}$ | $0.0110^{+0.0005}_{-0.0004}$ | $0.0520^{+0.0021}_{-0.0020}$ |
| n | 7.334 ± 0.093 | $2.57^{+0.15}_{-0.13}$ | $7.14^{+0.27}_{-0.48}$ | $0.709^{+0.049}_{-0.045}$ | $0.344^{+0.030}_{-0.029}$ |
| ϵ_1 | 0.0881 ± 0.0008 | $-0.099^{+0.011}_{-0.012}$ | $0.010^{+0.024}_{-0.023}$ | 0.039 ± 0.022 | $0.375^{+0.014}_{-0.015}$ |
| ϵ_2 | -0.0519 ± 0.0008 | -0.073 ± 0.017 | $-0.2564^{+0.027}_{-0.029}$ | -0.246 ± 0.017 | 0.402 ± 0.014 |
| x | -0.1814 ± 0.0009 | $0.0178^{+0.0080}_{-0.0083}$ | $-0.0307^{+0.0062}_{-0.0068}$ | $-0.0116^{+0.0070}_{-0.0074}$ | $-0.0228^{+0.0071}_{-0.0074}$ |
| y | -0.0893 ± 0.0009 | $-0.0553^{+0.0021}_{-0.0020}$ | 0.0171 ± 0.0025 | -0.0236 ± 0.0020 | $-0.0460^{+0.0021}_{-0.0022}$ |

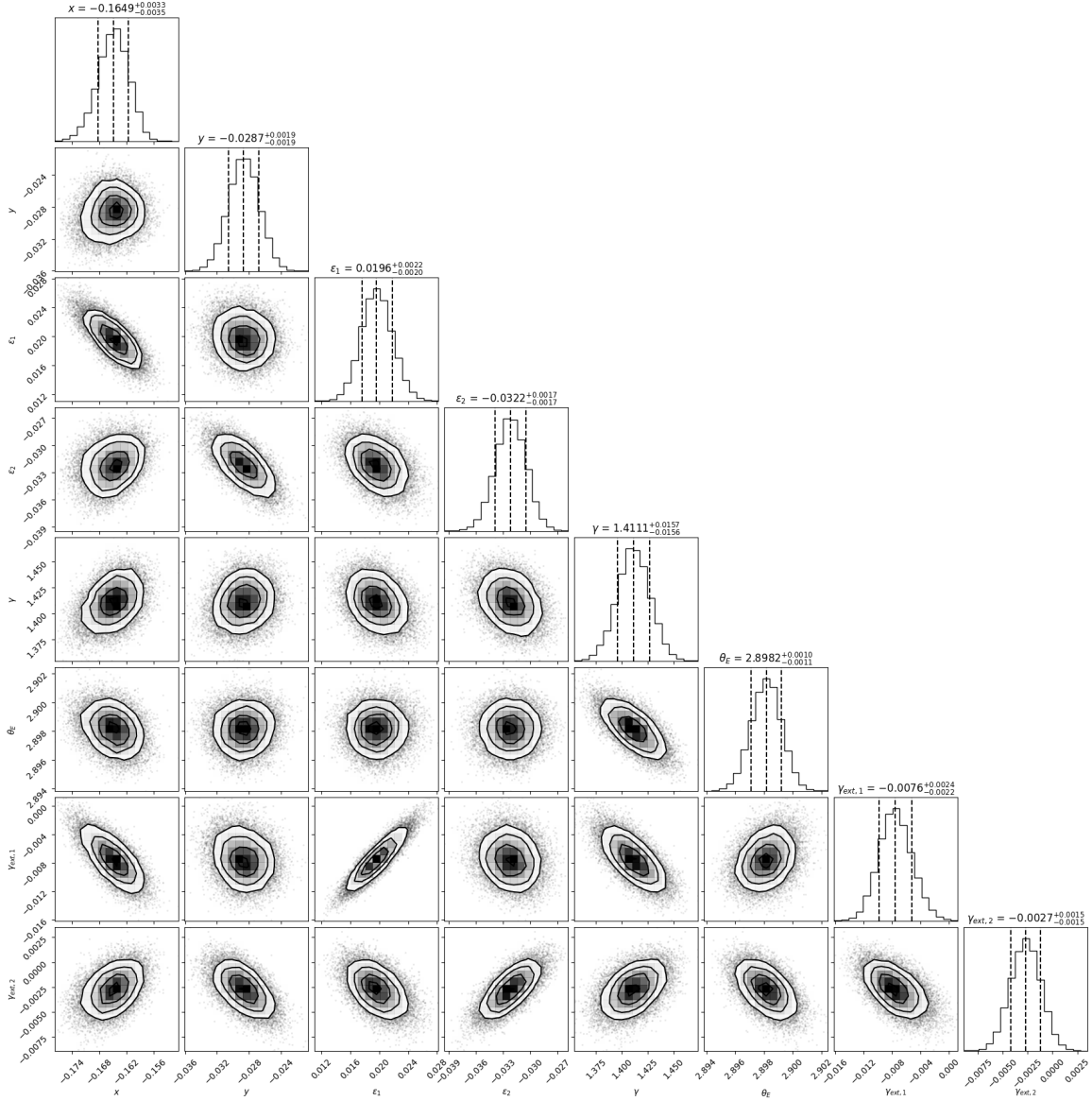


Figure 15. Corner plot for the eight mass parameters for DESI J154.6972-01.3590.

The \hat{R} values for all parameters satisfy the convergence criterion, $\hat{R} < 1.1$. In fact, the mean \hat{R} is 1.0011 and the maximum 1.0047.

From the HMC results, we estimate the magnification and the mass enclosed inside the critical curve. For the former, we use three different methods as described in the Appendix of Paper I. In particular, we computed the magnification for lensed images A (including the main lensed arc) and B separately (see Figure 13). The results appear in Table 10. We find the projected enclosed mass within the θ_E to be $M(< \theta_E) = 1.8203 \pm_{0.0014}^{0.0013} \times 10^{12} M_{\odot}$.

Table 10. Magnification calculations for DESI J154.6972-01.3590 using three approaches, for images A and B, and the total magnification, respectively.

| Method | A | B | Total |
|-----------------|---------------------------|---------------------------|----------------------------|
| 1 st | $88.88 \pm_{7.87}^{7.82}$ | $19.66 \pm_{1.86}^{1.59}$ | $108.55 \pm_{9.55}^{9.42}$ |
| 2 nd | $82.19 \pm_{7.87}^{7.27}$ | $21.83 \pm_{1.98}^{1.67}$ | $104.02 \pm_{9.95}^{8.74}$ |
| 3 rd | $80.85 \pm_{7.75}^{6.15}$ | $19.97 \pm_{2.00}^{1.56}$ | $100.82 \pm_{9.87}^{7.57}$ |

B.2. *DESI J165.6876-06.0423*

DESI J165.6876-06.0423 was discovered in H21 and modeled in Paper I. Based on color and photo- z , this galaxy appears to be at the center, and the brightest member, of a small group. The lens and source redshifts are $z_d = 0.4834$ and $z_s = 1.6748$. The Legacy Surveys image of DESI J165.6876-06.0423 shows an elliptical galaxy surrounded by what appears to be an almost complete Einstein ring, with the *HST* image revealing that it is a quadruply lensed system. Similar to five other systems in this work (with the exception of DESI J154.6972-01.3590), we used a 27×27 pixel empirical PSF. Our mass model comprises an elliptical power law (EPL) for the main lens with external shear. We model the lens light with two elliptical Sérsic profiles, and the source light with an elliptical Sérsic profile and a shapelets with $n_{max} = 6$ (Birrer et al. 2015). We determined the Einstein radius to be $\theta_E = 2.646 \pm 0.002''$, the slope of the power-law mass profile, $\gamma = 1.37 \pm 0.02$, and the total mass within the critical curve, $M(< \theta_E) = 1.7390_{-0.0043}^{+0.0046} \times 10^{12} M_\odot$. All \hat{R} values are below 1.06. It is one of three systems in which even an environmental galaxy is included in the full forward modeling. For more details, we refer the reader to Paper I.

B.3. *DESI J094.5639+50.3059*

DESI J094.5639+50.3059 was discovered in H21, with a ResNet probability of 1.000, and a human grade of A. The spectroscopic lens redshift, $z_d = 0.552$ is from Lick and DESI and source redshift, $z_s = 3.3332$, from Keck NIRES (both were reported in Paper III).

Figure 16 shows DESI J094.5639+50.3059 in a cutout with 120 pixels on the side. The image consists of a foreground elliptical galaxy with a large lensed arc and a counter-arc on the opposite side of the lens. There is also a small environmental galaxy towards the lower left of the main arc (arrow in Figure 16). As with DESI J154.6972-01.3590, we will refer to this object as the nearby galaxy. We also identify and mask out several faint objects in the cutout image (circles in Figure 16).

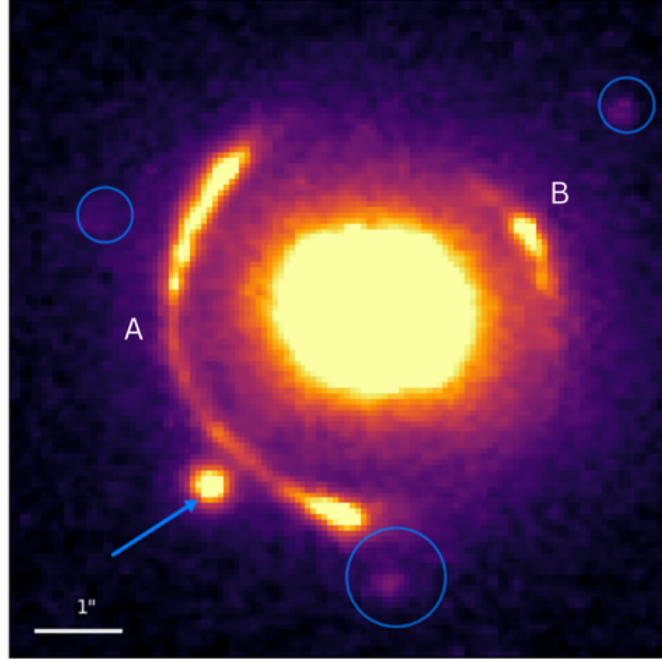


Figure 16. *HST* image of DESI J094.5639+50.3059. Faint objects circled in blue are masked out and not modeled. We model the light of the small environmental galaxy (arrow) and then fix its parameters.

This system is challenging to model due to several factors. First, its Einstein radius of around $\theta_E \approx 2.3''$ is relatively large. Furthermore, we find that a single Sérsic profile is inadequate for modeling the source. Lastly, the light of the bright environmental galaxy (arrow in Figure 16) overlaps slightly with the lensed image.

The lens light is modeled with two Sérsic profiles, and the source light with three Sérsic's. We model the light of the nearby galaxy separately, ahead of the main modeling process, using a Sérsic profile. We then fix its parameters.

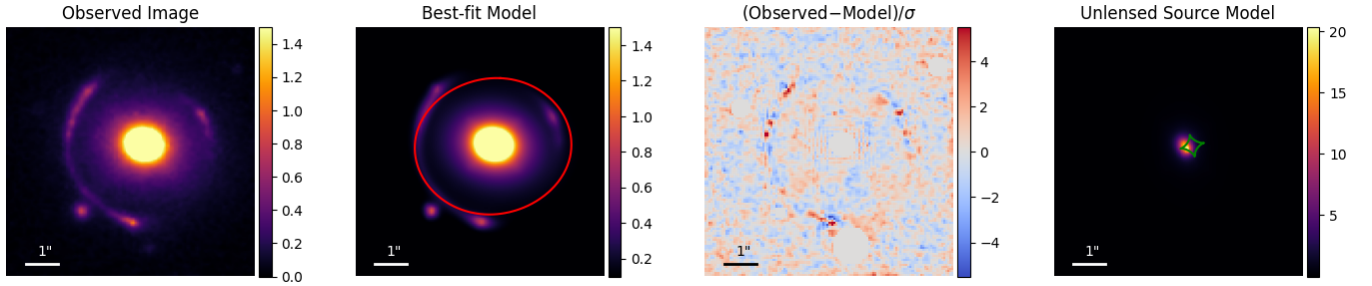
For the HMC step, the \hat{R} values for all parameters are below 1.1; in fact, the average \hat{R} is 1.02. The best-fit mass parameter for the lens appear in Table 11, and their sampled posterior distribution in Figure 18. We also show the best-fit values for the light parameters in Table 12. We achieve a reduced χ^2 of 1.049 (Figure 17).

Table 11. Best-fit mass parameters for DESI J094.5639+50.3059.

| θ_E | γ | ϵ_1 | ϵ_2 | x | y | $\gamma_{ext,1}$ | $\gamma_{ext,2}$ |
|---------------------|---------------------------|------------------------------|-------------------------------|---------------------|---------------------|----------------------|-------------------------------|
| 2.2866 ± 0.0004 | $2.540^{+0.043}_{-0.040}$ | $0.0633^{+0.0068}_{-0.0060}$ | $-0.0980^{+0.0073}_{-0.0089}$ | 0.4234 ± 0.0015 | 0.1215 ± 0.0010 | -0.0274 ± 0.0019 | $-0.0648^{+0.0013}_{-0.0012}$ |

Table 12. Best-fit light parameters for DESI J094.5639+50.3059

| Parameter | Lens light | | Source light | | |
|--------------|------------------------------|-------------------------------|------------------------------|------------------------------|------------------------------|
| | Comp 1 | Comp 2 | Comp 1 | Comp 2 | Comp 3 |
| R_e | $2.032^{+0.038}_{-0.028}$ | $1.413^{+0.055}_{-0.095}$ | $0.658^{+0.068}_{-0.061}$ | $0.544^{+0.051}_{-0.047}$ | $0.623^{+0.055}_{-0.050}$ |
| n | $0.531^{+0.079}_{-0.025}$ | $7.43^{+0.12}_{-0.14}$ | $9.24^{+0.54}_{-0.79}$ | $9.75^{+0.18}_{-0.34}$ | 2.40 ± 0.10 |
| ϵ_1 | $0.0090^{+0.0099}_{-0.0076}$ | $0.1060^{+0.0012}_{-0.0011}$ | -0.141 ± 0.018 | $-0.257^{+0.016}_{-0.015}$ | $-0.288^{+0.024}_{-0.023}$ |
| ϵ_2 | $0.084^{+0.010}_{-0.011}$ | $-0.0553^{+0.0012}_{-0.0014}$ | $0.2974^{+0.0019}_{-0.0042}$ | 0.083 ± 0.014 | $0.170^{+0.017}_{-0.018}$ |
| x | 0.571 ± 0.012 | $0.4700^{+0.0007}_{-0.0008}$ | $0.2595^{+0.0047}_{-0.0048}$ | $0.3210^{+0.0031}_{-0.0033}$ | $0.3577^{+0.0023}_{-0.0026}$ |
| y | $0.002^{+0.025}_{-0.016}$ | $0.1846^{+0.0007}_{-0.0006}$ | $0.1595^{+0.0013}_{-0.0012}$ | $0.0235^{+0.0036}_{-0.0037}$ | $0.0955^{+0.0017}_{-0.0019}$ |


Figure 17. Best Fit Model DESI J094.5639+50.3059. From left to right, we show: the observed Hubble image, our best-fit model with critical curve, the reduced residual, and the unlensed source with caustic.

Magnifications are computed for lensed images A (including the main lensed arc) and B separately (Figure 16). The results appear in Table 13. Finally, we found the projected mass within θ_E to be $M(< \theta_E) = 1.1231 \pm 0.0023 \times 10^{12} M_\odot$.

Table 13. Magnification calculations for DESI J094.5639+50.3059 using three approaches, for images A and B, and the total magnification, respectively.

| Method | A | B | Total |
|-----------------|------------------------|-------------------------|-------------------------|
| 1 st | $2.58^{+0.11}_{-0.13}$ | $9.30^{+0.92}_{-1.21}$ | $11.88^{+1.03}_{-1.34}$ |
| 2 nd | $2.34^{+0.16}_{-0.20}$ | $12.86^{+1.01}_{-1.25}$ | $15.20^{+1.17}_{-1.45}$ |
| 3 rd | $2.98^{+0.09}_{-0.14}$ | $11.68^{+1.10}_{-1.15}$ | 14.66 ± 1.19 |

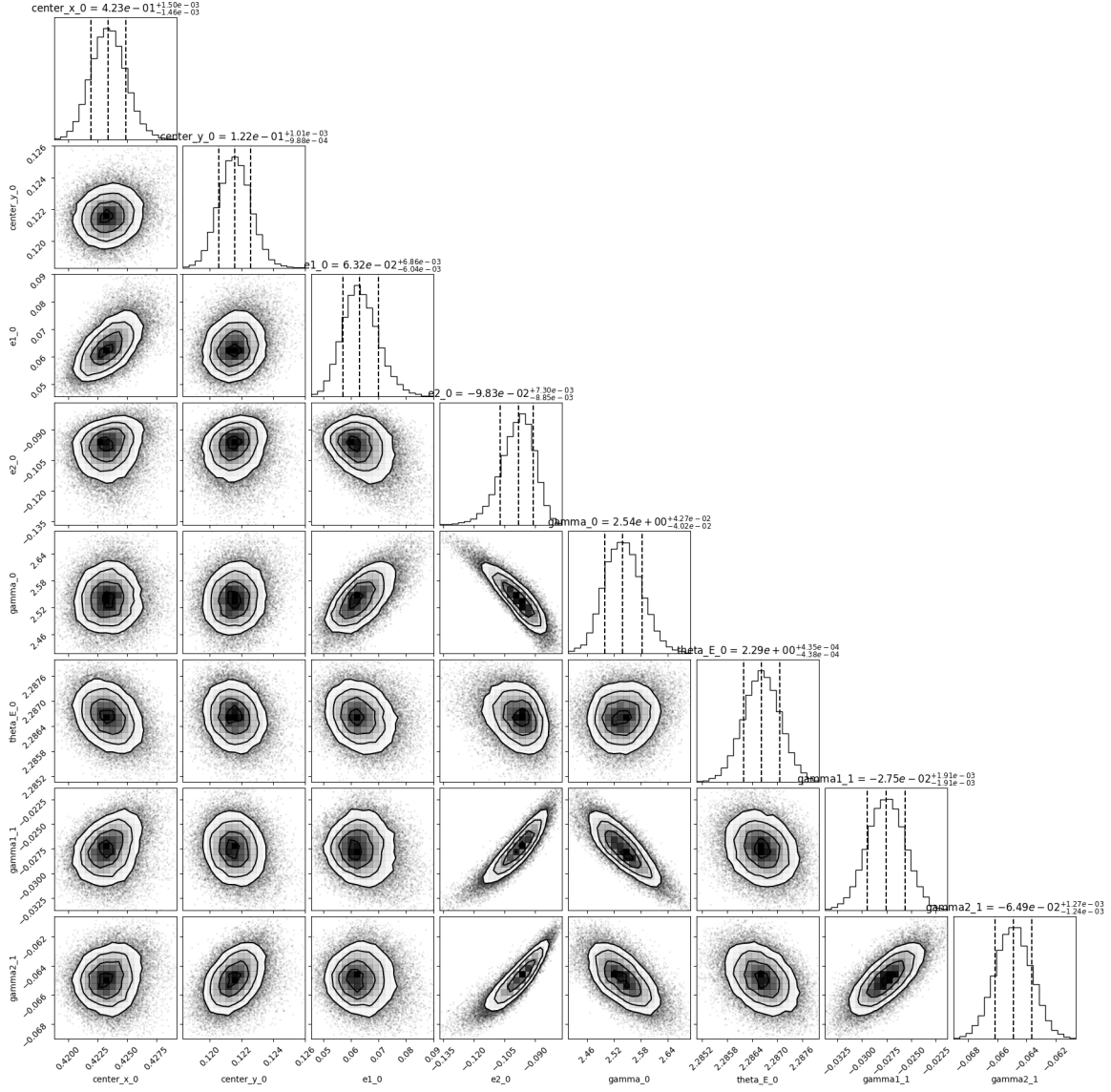


Figure 18. Sampled posterior distribution of mass parameters for system DESI J094.5639+50.3059.

B.4. *DESI J257.4348+31.9046*

[DESI J257.4348+31.9046](#) was discovered in H21, with a numerical grade of 3.0 (out of 4), corresponding to a B grade. The lens and source redshifts of $z_d = 0.7464$ and $z_s = 2.1200$ are obtained from DESI and Keck NIRES, respectively (Paper III). The Legacy Surveys image of this system shows an elliptical galaxy surrounded by an arc-counterarc pair, with an Einstein radius of approximately $\sim 2''$. The *HST* image resolves the main arc to be triple images, labeled as A (encompassing two merging images) and B, with the counter image labeled as C (Figure 19).

There is a very faint object south of the lensing system (small blue circle in Figure 19). This object is masked during the modeling process. We also mask the brightest part of a diffraction spike (from a bright star, indicated by the big blue circle in Figure 19) that extends to the vicinity of image C. The mask has a brightness threshold of $2\times$ the background noise. We use a 33×33 pixel empirical PSF, generated using the procedure outlined in Section A.

We model the lens light with two elliptical Sérsic profiles. The source is modeled using an elliptical Sérsic profile and a shapelets component with $n_{max} = 3$ (Birrer et al. 2015).

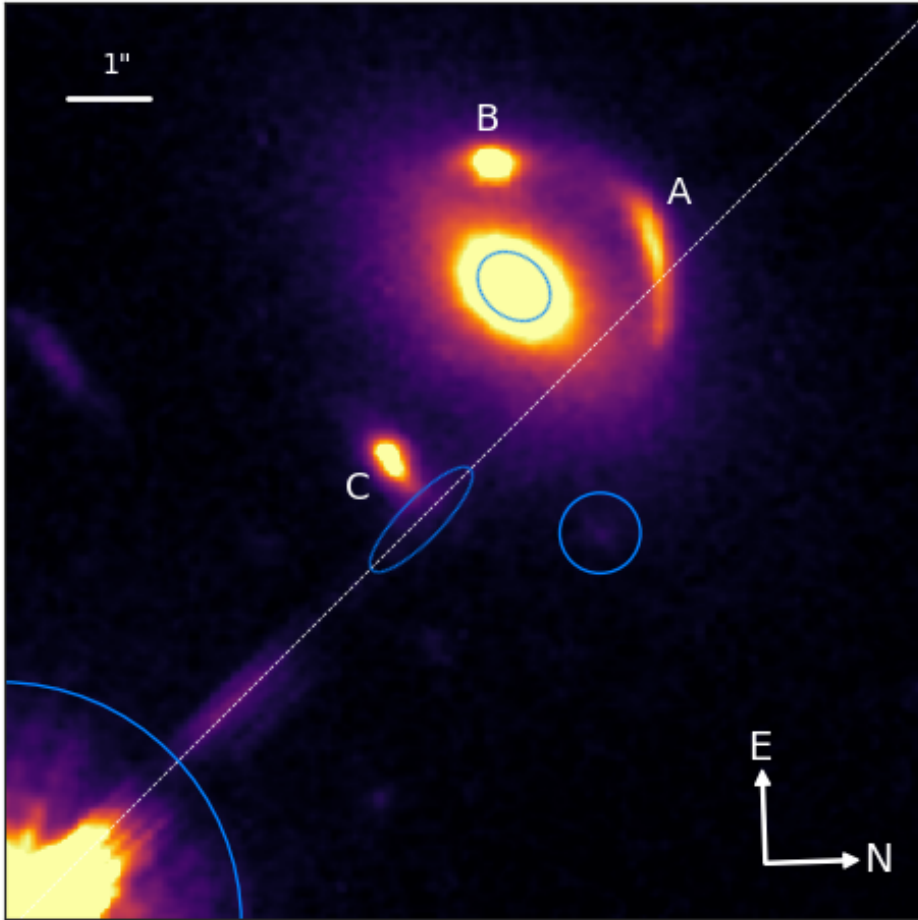


Figure 19. DESI J257.4348+31.9046. The three lensed images are labeled counterclockwise as A, B and C. To model this system, we mask out the light from a faint object in the bottom right corner (circle) and the brightest part of its diffraction spike (blue ellipse aligned with the dashed white line).

This system is modeled using linear inversion to solve for the light intensities. Our best-fit model, with a reduced χ^2 of 0.813, is shown in Figure 20. The best-fit mass and light parameters after HMC are shown in Tables 14 and 15 respectively.

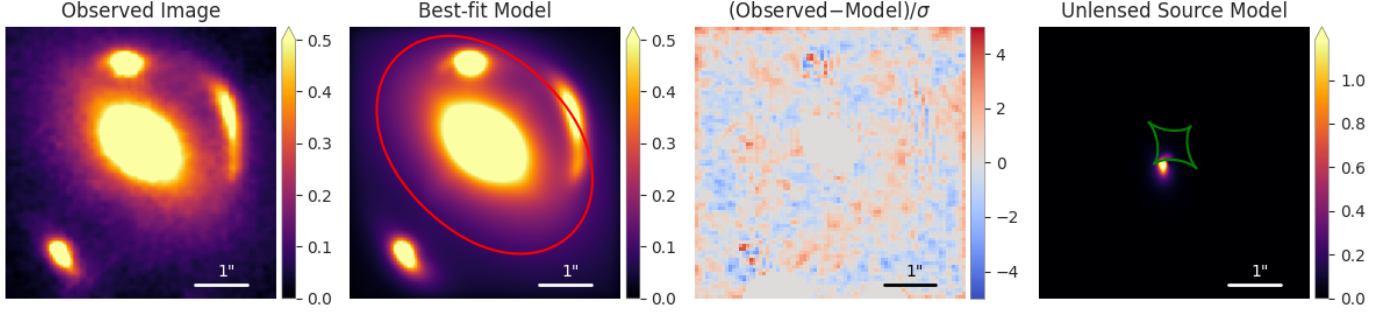


Figure 20. Best Fit Model for DESI J257.4348+31.9046. From left to right, we show: the observed Hubble image, our best-fit model with critical curve, the reduced residual, and the unlensed source with caustic.

Table 14. Best-fit mass parameters for DESI J257.4348+31.9046.

| θ_E | γ | ϵ_1 | ϵ_2 | x | y | $\gamma_{ext,1}$ | $\gamma_{ext,2}$ |
|---------------------|-------------------|----------------------|-------------------------------|-------------------------------|------------------------------|----------------------|---------------------|
| 1.9899 ± 0.0024 | 2.066 ± 0.023 | -0.0162 ± 0.0028 | $-0.1408^{+0.0064}_{-0.0066}$ | $-0.0111^{+0.0029}_{-0.0030}$ | $0.3386^{+0.0039}_{-0.0038}$ | -0.0148 ± 0.0015 | 0.0520 ± 0.0043 |

Table 15. Best-fit light parameters for DESI J257.4348+31.9046.

| Parameter | Lens light | | Source light | |
|---------------|-------------------------------|---------------------------|-------------------------------|-------------------------------|
| | Comp 1 | Comp 2 | Comp 1 | Comp 2 |
| R_e | $1.973^{+0.028}_{-0.027}$ | $0.241^{+0.012}_{-0.011}$ | $0.2146^{+0.0080}_{-0.0075}$ | - |
| n | $1.207^{+0.060}_{-0.056}$ | 2.78 ± 0.12 | $2.096^{+0.099}_{-0.093}$ | - |
| ϵ_1 | $0.0243^{+0.0025}_{-0.0026}$ | 0.0711 ± 0.0024 | -0.2242 ± 0.0077 | - |
| ϵ_2 | $-0.2345^{+0.0023}_{-0.0022}$ | -0.2387 ± 0.0022 | -0.0469 ± 0.0098 | - |
| x | $0.0422^{+0.0047}_{-0.0044}$ | -0.0132 ± 0.0005 | -0.2156 ± 0.0047 | $-0.1861^{+0.0045}_{-0.0043}$ |
| y | $0.3445^{+0.0036}_{-0.0038}$ | 0.3817 ± 0.0004 | $-0.1539^{+0.0095}_{-0.0098}$ | $0.0393^{+0.0065}_{-0.0068}$ |
| β_{shp} | - | - | - | 0.0495 ± 0.0011 |

We successfully sampled this system with \hat{R} values well below 1.01 for all parameters, achieving an average \hat{R} of 1.0002, with the maximum being 1.0012.

The mass parameter corner plot is shown in Fig. 21 and the magnification results are presented in Table 16. The total mass within the critical curve is $M(< \theta_E) = 1.5140^{+0.0074}_{-0.0078} \times 10^{12} M_\odot$.

Table 16. Magnification estimates for DESI J257.4348+31.9046 using three methods. Values are shown for images A through C.

| Method | A | B | C | Total |
|-----------------|----------------|-----------------|-----------------|----------------|
| 1 st | 22.7 ± 2.7 | 3.21 ± 0.26 | 2.71 ± 0.22 | 28.6 ± 2.7 |
| 2 nd | 18.9 ± 1.7 | 3.09 ± 0.28 | 2.57 ± 0.21 | 24.6 ± 1.7 |
| 3 rd | 20.4 ± 2.3 | 3.16 ± 0.29 | 2.64 ± 0.19 | 26.2 ± 2.3 |

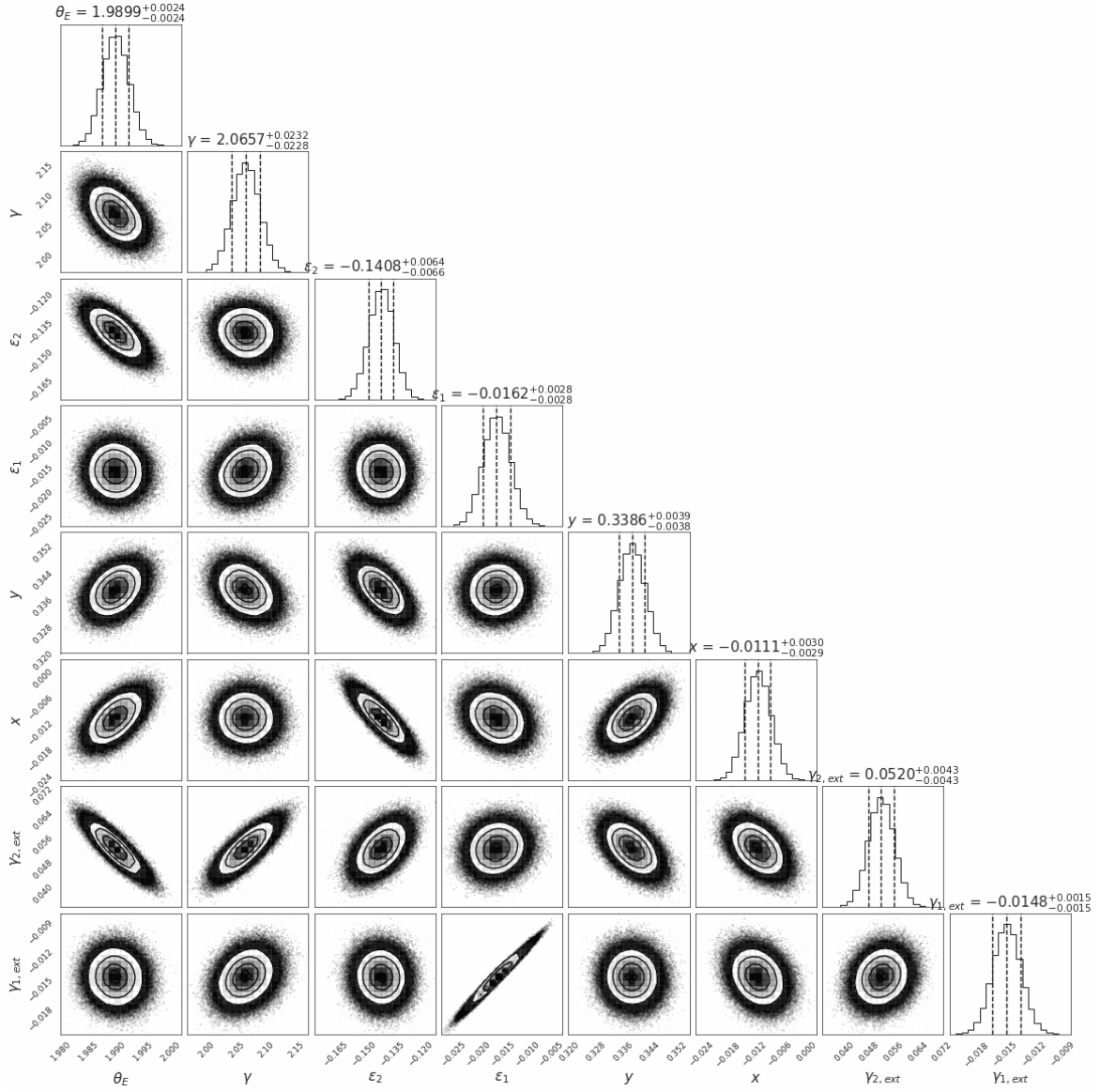


Figure 21. Corner plot for 8 mass parameters for DESI J257.4348+31.9046.

B.5. *DESI J246.0062+01.4836*

DESI J246.0062+01.4836 was discovered in H21, with a ResNet probability of 1.00, and a human score of 3.5 (out of 4.0), corresponding to an A grade. The lens redshift, $z_d=1.092$, is obtained from VLT/MUSE, based on the 4000 Å break and Ca H&K (Lin et al. 2025, Paper VI). This is one of the highest lens redshift galaxy-scale strong lensing systems (Koopmans & Treu 2002, $z_d=1.004$). This is certainly the highest lens redshift among the confirmed systems in the DESI Strong Lens Foundry project thus far. The source redshift, $z_s=2.368$, was first determined from Keck NIRES spectra (Paper III). In Paper IV, we further identify multiple weak absorption lines for different parts of the arc and thus show that they belong to the same source.

The lensing galaxy appears to be at the center and is the brightest member of a small galaxy group (Figure 23). This system has an Einstein radius of around $\theta_E \approx 2.7''$. We use a 31×31 pixel empirical PSF, generated using the procedure outlined in Section A.

We model the lens light with an elliptical Sérsic profile. We mask out a region around its center with a flux threshold of 0.40, as the central region of an elliptical galaxy is not always well described by a Sérsic profile (see, e.g., Paper I; Shajib et al. 2020). We model the source using five elliptical Sérsic profiles. This system has the most complex source structure (Figure 23) in this work.

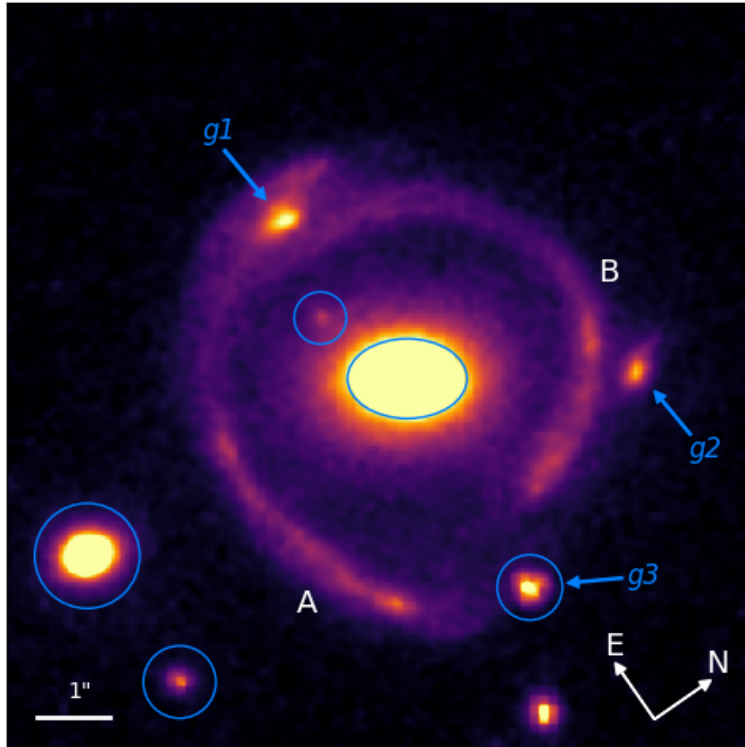


Figure 23. DESI J246.0062+01.4836. The two lensed arcs are labeled as A and B. To model this system, we mask out the light from the central region of the lensing galaxy (oval). We further mask out one faint galaxy to the upper left of the lensing galaxy and two galaxies near the lower left corner (all three are marked with circles). For g_1 , g_2 , and g_3 (arrows), we model their light and fix their parameters in the subsequent main modeling process. g_3 is also also circled because we mask out its central region.

We now briefly discuss the objects $g1$, $g2$, and $g3$ (Figure 23). From MUSE data (Paper VI), for $g1$, it is possible that we have detected the O II doublet ($\lambda\lambda$ 3726, 3729 Å). If this is a real detection, $g1$ is at a redshift of 1.07. For $g2$, we determine its redshift to be 1.441 based on a convincingly detected O II doublet. For $g3$, the spectrum does not have clear enough emission or absorption features for us to securely determine its redshift. However, the MUSE image has a slightly better seeing than the Legacy Surveys, and as a result, $g3$ is deblended from the lensed arc, and it clearly has a different color from the lensed arcs, and thus is not part of them. In addition, based on the surface brightness, $g1$ does not appear to be part of the lensed arcs either. In this work, we model the light of $g1$ with two elliptical Sérsic's. For each of $g2$ and $g3$, we use an elliptical Sérsic profile. Then, we freeze these 28 parameters. We further mask out the central region of $g3$. It is possible that modeling the mass of $g1$ and $g2$ will further improve the model. We leave this for further work.

In addition, we mask a small and dim object (small blue circle just to the east of the main lens in Figure 23; note the orientation of the compass). We also mask two objects near the bottom left corner. We determine the brighter of the two, from the MUSE datacube, to be a group member, based on the 4000 Å break and Ca H&K absorption (Paper VI).

For the modeling of DESI J246.0062+01.4836, we do not use linear inversion to solve for the light intensities for this system. Instead, we explicitly fit for the light intensities (I_e). For the Sérsic index (n_s) of the first source light component, we initially used a lower bound of 0.5 (Gu22). However, in the modeling process, we find that this parameter is consistently pushed towards its lower limit. When we lower the lower bound to 0.2, this behavior stops. We find the best-fit value for n_s of the first source component to be $0.234^{+0.016}_{-0.15}$. We note that Tamm & Tenjes (2006) reported a similarly low $n_s = 0.3 \pm 0.05$ for a galaxy. Moreover, this is just one component of the source light, which as we show below has a complex structure.

To achieve convergence in a reasonable amount of time, we freeze the 28 parameters describing the environmental galaxies $g1$, $g2$, and $g3$. It is important to note that these belong to neither the lens nor the source. We do not observe significant correlation between the mass parameters of the main lens (the main goal of the lens modeling effort) and these fixed parameters.

In modeling this system, we have significantly advanced the frontier of galaxy-scale strong lens modeling: this is a system with a large θ_E , very complex source structure, and a large number of environmental galaxies in the cutout, which, given the large cutout, is not unexpected. In our model, we simultaneously optimize and sample 50 parameters! To the best of our knowledge, for a galaxy-scale strong lens, this is unprecedented.

We achieve very good residuals (Figure 24), with a reduced $\chi^2 = 1.1299$. The central region of $g3$ is masked when displaying the residuals and computing χ^2 , but not during the modeling process. We present the best-fit mass parameters in Table 17, and light parameters in 18. We show the five Sérsic components for the source in Figure 25.

We successfully sampled this system with \hat{R} values well below 1.1 for all parameters, achieving an average \hat{R} of 1.003, with the maximum being 1.037.

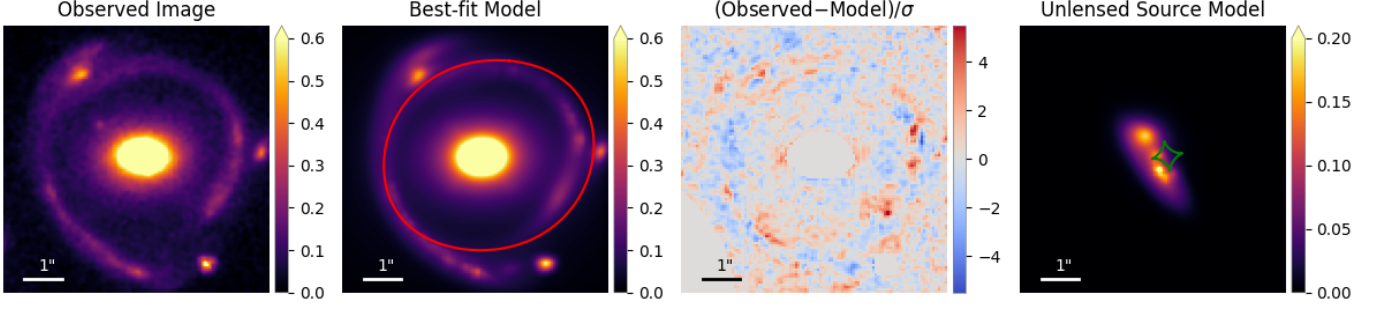


Figure 24. Best Fit Model for DESI-246.0062+01.4836. From left to right, we show: the observed Hubble image, our best-fit model with critical curve, the reduced residual, and the unlensed source with caustic.

Notably, each Sérsic component contributes to both arcs. This consistency reinforces the reliability of our results, as the five components align coherently, indicating that they belong to the same object.

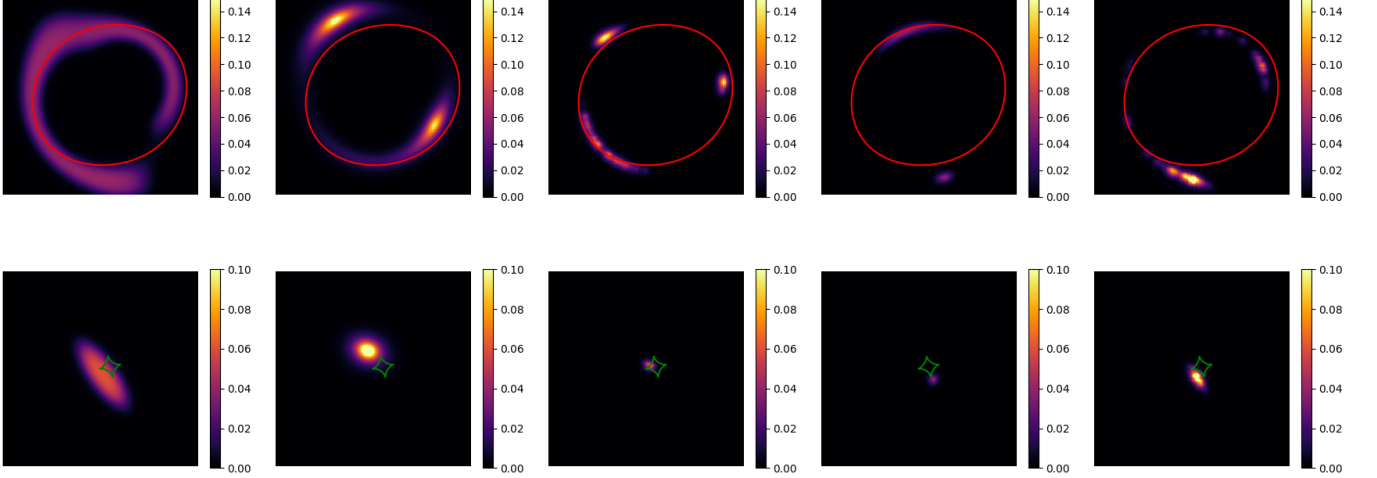


Figure 25. Source light Sérsic components in the lensed (top row) and unlensed (bottom row) plane for DESI J246.0062+01.4836. We label them as component 1 to 5 from left to right.

Table 17. Best-fit mass parameters for DESI-246.0062+01.4836.

| θ_E | γ | ϵ_1 | ϵ_2 | x | y | $\gamma_{ext,1}$ | $\gamma_{ext,2}$ |
|---------------------|-------------------|------------------------------|------------------------------|---------------------|---------------------|----------------------|------------------------------|
| 2.6982 ± 0.0007 | 2.616 ± 0.017 | $0.0537^{+0.0029}_{-0.0027}$ | $0.1789^{+0.0070}_{-0.0069}$ | 0.3664 ± 0.0007 | 0.1028 ± 0.0006 | -0.0521 ± 0.0006 | $0.0307^{+0.0004}_{-0.0005}$ |

Table 18. Best-fit light parameters for DESI-246.0062+01.4836.

| Parameter | Lens light | Source light | | | | |
|--------------|---------------------------|-------------------------------|------------------------------|-------------------------------|-------------------------------|-------------------------------|
| | | Comp 1 | Comp 2 | Comp 3 | Comp 4 | Comp 5 |
| R_e | $2.158^{+0.096}_{-0.090}$ | $0.5005^{+0.010}_{-0.012}$ | $0.3464^{+0.0076}_{-0.0072}$ | $0.0345^{+0.0010}_{-0.0009}$ | $0.0671^{+0.0048}_{-0.0043}$ | 0.0356 ± 0.0008 |
| n | $6.97^{+0.32}_{-0.31}$ | $0.234^{+0.016}_{-0.015}$ | $1.046^{+0.048}_{-0.046}$ | $0.527^{+0.056}_{-0.050}$ | $0.522^{+0.037}_{-0.017}$ | $0.644^{+0.062}_{-0.054}$ |
| ϵ_1 | 0.1749 ± 0.0017 | $-0.1645 \pm +0.0085$ | $0.114 \pm +0.011$ | $0.5149^{+0.0087}_{-0.0088}$ | $-0.148^{+0.054}_{-0.051}$ | -0.4395 ± 0.0038 |
| ϵ_2 | 0.0085 ± 0.0016 | $-0.4660^{+0.0065}_{-0.0064}$ | -0.101 ± 0.015 | $-0.5955^{+0.0062}_{-0.0033}$ | 0.0239 ± 0.047 | $-0.8516^{+0.0032}_{-0.0029}$ |
| x | 0.1885 ± 0.0019 | 0.094 ± 0.010 | -0.1945 ± 0.0086 | 0.1222 ± 0.0031 | $0.5136^{+0.0041}_{-0.0039}$ | $0.2042^{+0.0025}_{-0.0026}$ |
| y | 0.063 ± 0.0013 | $-0.227^{+0.016}_{-0.017}$ | $0.6497^{+0.0059}_{-0.0060}$ | 0.1110 ± 0.0017 | $-0.3990^{+0.0094}_{-0.0095}$ | $-0.3530^{+0.0069}_{-0.0066}$ |
| I_e | $10.50^{+0.87}_{-0.83}$ | $11.59^{+0.27}_{-0.26}$ | 11.93 ± 0.52 | 143 ± 7.8 | $23.0^{+2.3}_{-2.1}$ | 462^{+29}_{-27} |

The corner plot for the mass parameters is displayed in Figure 26. The best-fit Einstein radius is $\theta_E = 2.6982'' \pm 0.0007$, and the mass profile slope, $\gamma = 2.616 \pm 0.017$. The projected total mass within the critical curve is $M(< \theta_E) = 4.0735^{+0.0109}_{-0.0089} \times 10^{12} M_\odot$. The magnification results for each of the three methods are shown in Table 19.

Table 19. Magnification estimates for DESI J246.0062+01.4836 using three methods. Values are shown for components A and B.

| Method | A | B | Total |
|-----------------|-----------------|-----------------|----------------|
| 1 st | 7.60 ± 1.79 | 2.87 ± 0.54 | 10.1 ± 1.9 |
| 2 nd | 5.50 ± 1.63 | 2.11 ± 0.54 | 7.6 ± 1.7 |
| 3 rd | 6.2 ± 1.4 | 2.51 ± 0.52 | 8.7 ± 1.5 |

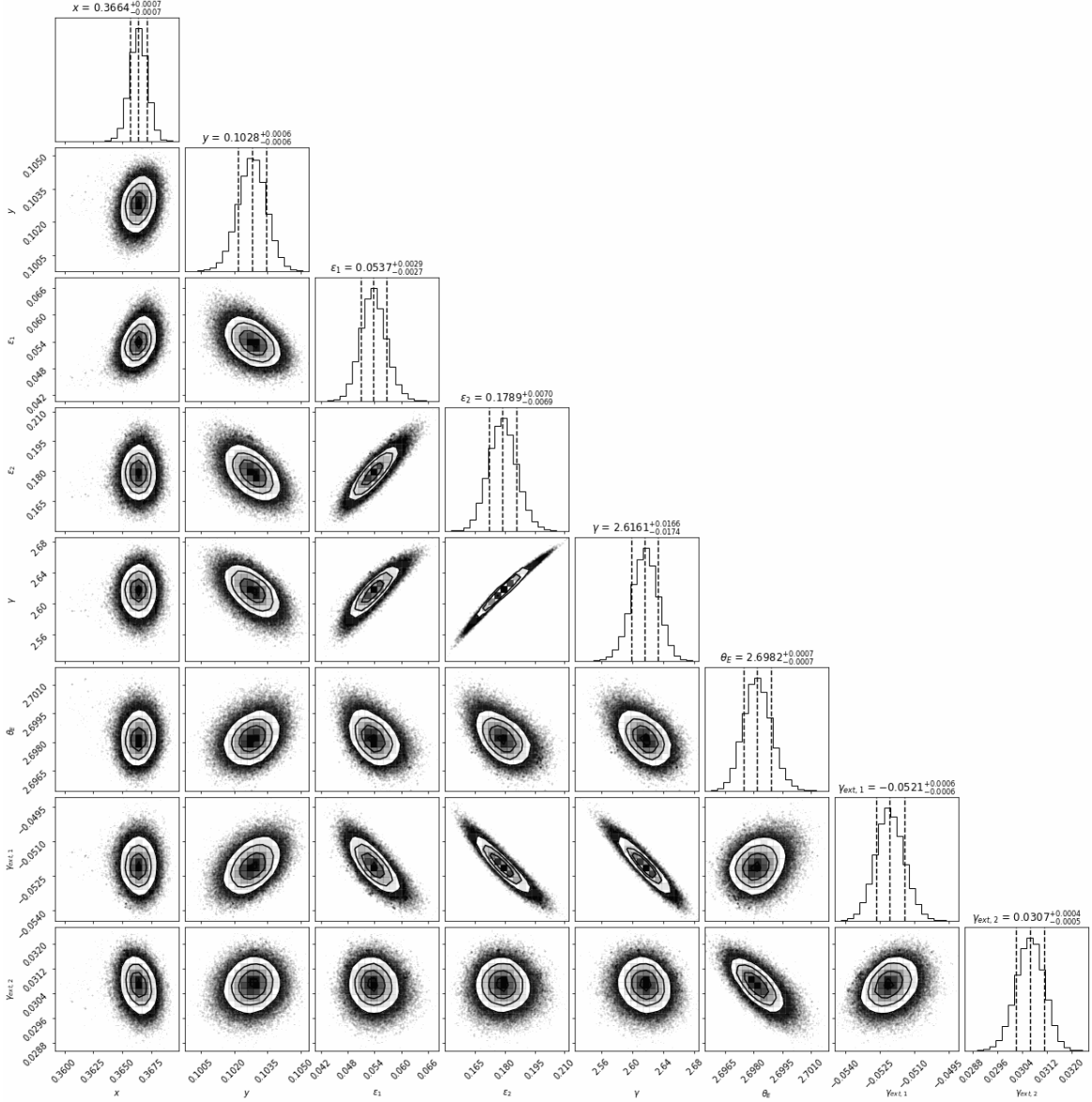


Figure 26. Corner plot for the eight mass parameters for DESI J246.0062+01.4836.

C. CONVERGENCE METRICS

C.1. \hat{R} Definitional Differences

Following Brooks & Gelman (1998, BG98), Equation (1.1)

$$\hat{R}_{BG98} = \frac{\hat{V}}{W} \quad (\text{C1})$$

with

$$\hat{V} = \hat{\sigma}_+^2 + \frac{B}{mn} \quad (\text{C2})$$

and

$$\hat{\sigma}_+^2 = \frac{n-1}{n}W + \frac{B}{n} \quad (\text{C3})$$

where m is the number of chains and n is the number of samples.

The definition of $\hat{\sigma}_+^2$ (Equation C3) is the same as in Gelman et al. (2014, G14), Equation (11.3), written as $\widehat{\text{var}}^+$. The definitions of W and B (not given here) are also the same in BG98 and G14.

In G14, \hat{R} is defined as the following, in their Equation (11.4),

$$\hat{R}_{G14} = \sqrt{\frac{\widehat{\text{var}}^+}{W}} \quad (\text{C4})$$

Comparing Equations C1 and C4, which are the definitions of \hat{R} in BG98 and G14, respectively, there are two differences. First, BG98 deals with variances (as explicitly pointed out in their Section 1.2), thus no square root; whereas G14 deals with the actual “scale” (the “scale” in the Potential Scale Reduction Factor), and thus the square root is applied. Second, in BG98, there is an extra term in the numerator of the \hat{R} definition: $\frac{B}{mn}$ (the second term in Equation C2). The product of mn tends to be very large, and this represents a small correction. Therefore, the main difference results from whether the square root is applied.

The `TensorFlow` documentation states that using the BG98 definition, $\hat{R} < 1.2$ (without the square root) indicates approximate convergence⁸ (BG98, p. 444⁹). Gelman et al. (2014, G14) provides the current definition of \hat{R} , which is approximately the square root of the definition that BG98 (and `TensorFlow`) used.¹⁰ and the recommended threshold $\hat{R} < 1.1$ for convergence (G14, p. 287; consistent with BG98). This is the definition we use in this paper.

Finally, in Paper I, we used the G14 definition for \hat{R} . However, in Cikota et al. (2023), we used the BG98 definition (i.e., the \hat{R} value as reported by `TensorFlow`), without taking its square root — this was before we realized the definitional difference discussed in this section. Therefore, using the G14 definition of \hat{R} , all parameters in Cikota et al. (2023) are below the threshold of 1.1.

⁸ See https://www.tensorflow.org/probability/api_docs/python/tfp/mcmc/potential_scale_reduction

⁹ Somewhat confusingly, in Section 3.2 of BG98, when introducing the threshold of 1.2, they *put \hat{R} under the square root*. However, that does not change the fact that the definitions of \hat{R} in BG98 and G14 differ by the square root and that `TensorFlow` implemented the BG98 version without the square root.

¹⁰ See also the Stan Reference Manual Section 15.3.1, <https://mc-stan.org/docs/2.18/reference-manual/notation-for-samples-chains-and-draws.html>.